High-Q Superconducting Coplanar Waveguide Resonators for Integration into Molecule Ion Traps

by

Adam Nykoruk McCaughan

Submitted to the
Department of Electrical Engineering and Computer Science
in partial fulfillment of the requirements for the degree of

Master of Engineering in Electrical Engineering and Computer Science

at the

Massachusetts Institute of Technology

May 2010
[June 2010]
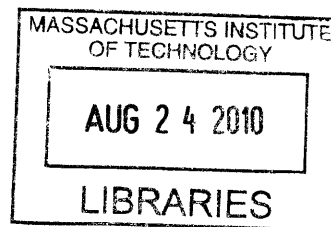
ARCHIVES

Author . . . .
Department of Electrical Engineering and Computer Science
May 21, 2010

Certified by . . . .
Karl K. Berggren
Associate Professor of Electrical Engineering
Thesis Supervisor

Accepted by . . . .
Christopher J. Terman
Chairman, Department Committee on Graduate Theses

		Form Approved OMB No. 0704-0188

Report Documentation Page

Form Approved
OMB No. 0704-0188

Public reporting burden for the collection of information is estimated to average 1 hour per response, including the time for reviewing instructions, searching existing data sources, gathering and maintaining the data needed, and completing and reviewing the collection of information. Send comments regarding this burden estimate or any other aspect of this collection of information, including suggestions for reducing this burden, to Washington Headquarters Services, Directorate for Information Operations and Reports, 1215 Jefferson Davis Highway, Suite 1204, Arlington VA 22202-4302. Respondents should be aware that notwithstanding any other provision of law, no person shall be subject to a penalty for failing to comply with a collection of information if it does not display a currently valid OMB control number.

1. REPORT DATE **MAY 2010**	2. REPORT TYPE	3. DATES COVERED **00-00-2010 to 00-00-2010**
4. TITLE AND SUBTITLE **High-Q Superconducting Coplanar Waveguide Resonators for Integration into Molecule Ion Traps**		5a. CONTRACT NUMBER
		5b. GRANT NUMBER
		5c. PROGRAM ELEMENT NUMBER
6. AUTHOR(S)		5d. PROJECT NUMBER
		5e. TASK NUMBER
		5f. WORK UNIT NUMBER
7. PERFORMING ORGANIZATION NAME(S) AND ADDRESS(ES) **Massachusetts Institute of Technology,77 Massachusetts Avenue,Cambridge,MA,02139**		8. PERFORMING ORGANIZATION REPORT NUMBER
9. SPONSORING/MONITORING AGENCY NAME(S) AND ADDRESS(ES)		10. SPONSOR/MONITOR'S ACRONYM(S)
		11. SPONSOR/MONITOR'S REPORT NUMBER(S)
12. DISTRIBUTION/AVAILABILITY STATEMENT **Approved for public release; distribution unlimited**		
13. SUPPLEMENTARY NOTES		

14. ABSTRACT

Over the last decade, quantum information experiments with trapped ions have demonstrated essential steps towards quantum computing and quantum simulation. Large fields are required to achieve strong coupling to the ions via dipolar interactions, and so we fabricated transmission line microresonators-capable of producing large fields in a standing wave at resonance-for eventual integration into 2D ion trap structures. The resonators were superconducting to minimize loss and maximize quality factor. We fabricated the resonators as two dimensional coplanar waveguides in niobium on R-plane sapphire using optical lithography. Resist was patterned on the niobium using optical lithography, developed then reactive-ion etched to transfer the pattern into the niobium. The resonators were cooled and tested in a cryogenic probe station and characterized with a network analyzer. Additionally, the resonator geometry was reproduced in commercial microwave simulation software. Results from our fabricated resonators showed first-resonance quality factors of 1.2x 104 at 3.23 GHz at device temperatures of 3-4 K.

15. SUBJECT TERMS					
16. SECURITY CLASSIFICATION OF:			17. LIMITATION OF ABSTRACT	18. NUMBER OF PAGES	19a. NAME OF RESPONSIBLE PERSON
a. REPORT **unclassified**	b. ABSTRACT **unclassified**	c. THIS PAGE **unclassified**	**Same as Report (SAR)**	**96**	

Standard Form 298 (Rev. 8-98)
Prescribed by ANSI Std Z39-18

High-Q Superconducting Coplanar Waveguide Resonators for Integration into Molecule Ion Traps

by

Adam Nykoruk McCaughan

Submitted to the
Department of Electrical Engineering and Computer Science
on May 21, 2010
in partial fulfillment of the requirements for the degree of
Master of Engineering in Electrical Engineering and Computer Science

Abstract

Over the last decade, quantum information experiments with trapped ions have demonstrated essential steps towards quantum computing and quantum simulation. Large fields are required to achieve strong coupling to the ions via dipolar interactions, and so we fabricated transmission line microresonators–capable of producing large fields in a standing wave at resonance–for eventual integration into 2D ion trap structures. The resonators were superconducting to minimize loss and maximize quality factor. We fabricated the resonators as two dimensional coplanar waveguides in niobium on R-plane sapphire using optical lithography. Resist was patterned on the niobium using optical lithography, developed, then reactive-ion etched to transfer the pattern into the niobium. The resonators were cooled and tested in a cryogenic probe station and characterized with a network analyzer. Additionally, the resonator geometry was reproduced in commercial microwave simulation software. Results from our fabricated resonators showed first-resonance quality factors of 1.2×10^4 at 3.23 GHz at device temperatures of 3-4 K.

Thesis Supervisor: Karl K. Berggren
Title: Associate Professor of Electrical Engineering

Acknowledgments

It has been a pleasure working with the Quantum Nanostructures and Nanofabrication group this past year. I am extremely grateful to all of my colleagues in the group for their continuing support and guidance.

First I would like to thank my advisor Professor Karl Berggren for giving me this great interdisciplinary opportunity, and helping me develop my skills as a researcher and experimentalist. His honest manner and focus on moving forward have helped keep me on track towards my research goals. I would also like to thank Professor Isaac Chuang, who early in the project gave me a lot of great advice about the nature of research.

I would also like to give a heartfelt thank you to Stephan Schulz for the countless hours he spent sharing knowledge and providing spirited responses to my questions. His experience and dedication stayed the course through those first uncertain months when the project was new, and I am certainly the better researcher now for having had him as a mentor. I wish him the best of luck at PTB in Germany.

David Meyer, although recent to the project, has already contributed greatly to its development and our understanding and I look forward to working with him in the coming years. I am also thankful that Diana Aude joined the effort, and impressed how deftly she took the resonator simulations into her own hands.

It's been a privilege to work with Faraz Najefi and Francesco Marsili, both intelligent, hard working researchers and also great people to joke around with. I'd also like to thank Yufei Ge and Eric Dauler for developing the materials processes I used, Paul Antohi for his insight and collaboration toward integrated traps, Jim Daley for his technical support in the NSL, and Rajeev Ram for the use of his group's probe station.

Last, but certainly not least, I'd like the thank my parents, my sister, and the members of my extended family and GF for their continuous love and support.

3

Contents

List of Figures

Chapter 1

Introduction

Resonators are one of the most fundamental types of passive circuit, and though they have been around for over a century, current research is still finding new uses for them. By scaling the size down using microfabrication techniques, it is possible to build resonators that operate in the microwave regime, extending their applications beyond the realm of their traditional place in lumped-element analog electronics. Recent applications include use in microwave kinetic-inductance detectors[29], multiplexed SQUIDs[10], and most pertinent to the work discussed in this thesis, ion trapping and quantum information processing.

1.1 Quantum Information Processing and Ion Trapping

Quantum information processing is a relatively new field that seeks to expand the realm of traditional computing by interfacing with quantum mechanical phenomena to build and measure quantum bits, or qubits. Algorithms already exist within the field that offer significant speedup to perform traditionally difficult tasks such as factoring large primes or searching large databases. A particularly promising way of building qubits for quantum computation comes in the field of ion trapping.

1.1.1 Ion trapping

Ion trapping comes in many forms, but recently there has been significant development in the area of planar ion trapping. A planar ion trap is functionally identical to a standard

8

linear RF Paul trap[17], in that it creates an oscillating quadrature electric field with a local minima able to capture ions in two dimensions[18]. The difference lies in the geometry of the trap, which adapts the confinement electrodes from their standard three-dimensional configuration into a two-dimensional planar structure.

Planar RF ion traps have many advantages over their 3D cousins. Most importantly, their planar structure allows for rapid prototyping with standard microfabrication techniques. Additionally, they hold promise as a scalable architecture, since any one trap may hold several ions, and multiple traps may be fabricated over a small area and potentially used as a network of processing and memory zones[23]. Lastly, they offer advantages in cryogenic ion trapping, such as the ion trapping currently being researched in MIT's Center for Ultracold Atoms (CUA).

1.1.2   Current ion trapping research at the CUA

We have previously demonstrated the ability to trap $^{88}Sr^+$ in the CUA using a cryogenic planar ion trap[2][3][12] with lifetimes of over 2500 min. Operation at cryogenic temperatures is particularly useful in ion trapping because of the high vacuum it generates–ion lifetime is typically cut short through interactions with residual gasses. The trap was planar both to simplify fabrication, and to allow contact of the trap substrate (and subsequently, electrodes) directly against the cooling stage of the cryostat in which the apparatus is tested. The strontium ions were laser ablated from a $SrTiO_3$ target, then Doppler and sideband cooled into the motional ground state for trapping. Once trapped, the ions were detected with an optical setup that observed their fluorescence.

1.2   Towards an Ion Trap with an Integrated Superconducting Resonator

Though trapping has already been demonstrated, we now seek to interact with the trapped particles and thus take a step towards quantum processing. Specifically, we hope to trap $SrCl_2$ molecules and excite their long-lived rotational states[1]. These molecules have a transition near 6 GHz, and so we should be able to demonstrate coupling by placing them

in a strong electric field oscillating at that transition frequency.

Rather than having to purchase a military-grade microwave source capable of generating hundreds of watts of microwave power to achieve this coupling, a transmission line cavity resonator can be used to accumulate microwave photons. Operated at resonance, the photons in the cavity form a standing wave with a high electric field (orders of magnitude larger than the source wave) at the field antinodes. By integrating a transmission line resonator into the planar trap geometry, we hope to be able to maneuver the ion near the localized nodes of high electric field and interact with it in the strong coupling regime.

1.2.1 Designing the resonator for our needs

As a building block towards the larger goal of quantum computation, this thesis is focused on the fabrication of suitable resonators for trap integration. Precisely how many photons are able to be trapped in the resonator cavity–and thus how high an electric field can be achieved–is determined by a critical parameter called the quality factor, or Q. We desired a high quality factor, and so the transmission line resonators described in this thesis were designed using a superconducting coplanar waveguide to minimize energy lost through dissipation in the metal and dielectric. The effects of superconductivity on the resonator as a whole and the quality factor are the subject of discussion in Chapter 3.

In Chapter 2 we describe the complete fabrication of superconducting niobium resonators designed to achieve very high quality factors with a first resonance at 3 GHz. The resonators are completely planar, and the process involves only the manipulation of a single niobium layer on a sapphire substrate. Briefly, the conductor layer is deposited, photoresist is patterned on its surface, and then the resist pattern is transferred into the conductor by means of reactive-ion etching.

The majority of the resonators fabricated were characterized using a cryogenic probe station and network analyzer. Information on the probe station, other apparatus, and procedures may be found in Chapter 5. Lastly, the results of of our work are explored in Chapter 6.

Chapter 2

Materials and Fabrication

This chapter details the processes developed in the production of our superconducting resonators. Much of the previous work done examining these devices was done with either aluminum or niobium as the superconductor, and silicon or sapphire as the dielectric substrate. Many factors affect the higher-order properties of superconducting resonators (such as kinetic inductance), but in terms of the first-order lumped-element model, the resonators may be fabricated out of any conductor and substrate combination. Since we began this investigation with no pre-existing devices to adapt, we opted to use materials which have both already been shown to produce high quality factors, and which we were able to fabricate from day one: niobium and sapphire. Since the expertise for depositing niobium films already existed within the group, we used the existing niobium process and built the remainder of our fabrication steps on top of that.

2.1 The Material Stack

Fabrication began with a 330μm thick, 5 cm crystalline R-plane sapphire wafer. The wafers were ordered from Kyocera Industrial Ceramics, and they were epitaxially polished on one side, and chemically polished on the other. Since the wafers were R-plane, they exhibited dielectric anisotropy between the two axes parallel with the cut of the wafer. These two axes were the A-axis and the C-axis, which according to the Kyocera data sheet had effective dielectric constants of 9.3 and 11.5 respectively. For our devices, all of our calculations were

done with regard to the C-axis. The reason for choosing the higher dielectric constant was to force more of the resonating field out of the sapphire, where the high dielectric constant made field density energetically expensive, and put more of the field into the surrounding vacuum, where it could interact with the ion.

Niobium was used primarily because the deposition capability for this material already existed within the lab. We additionally tried using niobium nitride, but NbN is highly variable in material phase and T_c[13][16], based on the temperature and gas ratio with which it is sputtered. Despite the higher critical temperature of NbN, we decided that the simpler material of niobium was the best route in the early stages of developing a high quality factor. Previous literature suggested niobium was a suitable superconductor for quality factors in the range of 10^6 - 10^7[9][11][5][22], and our probe station tests operated at around 3-4 K, well below the critical temperature of niobium. Additionally, we were advised by Dr. Ben Mazin not to bother with NbN, and that other issues such as sloping sidewalls were more critical to the resonator fabrication.

All of the primary deposition and fabrication was realized on the epi-polished side of the wafer, although the backside was also coated for purposes of heat conduction and to provide a ground layer. Niobiumwas deposited on the wafer by means of an AJA sputtering system[1] located in the Quantum Nanostructures and Nanofabrication Laboratory at MIT and shown in Figure 2-1. In the following subsections we describe the procedure used to deposit niobium in the AJA sputtering system and build the Nb-sapphire-Nb "material stack."

2.2 Resonator Fabrication

The process began by first coating the backside of the wafer with a thin film of sputtered niobium from a 99.95% pure target. This layer was never patterned, and was only necessary to help the wafer absorb thermal radiation from the hot chuck when the polished side was being coated. In the following paragraphs, the backside coating procedure is neglected for the more complete frontside coating procedure, but is detailed afterwards. A wafer cleaning

---

[1]Model ATC 2000 thin film deposition system, built by AJA International, Inc
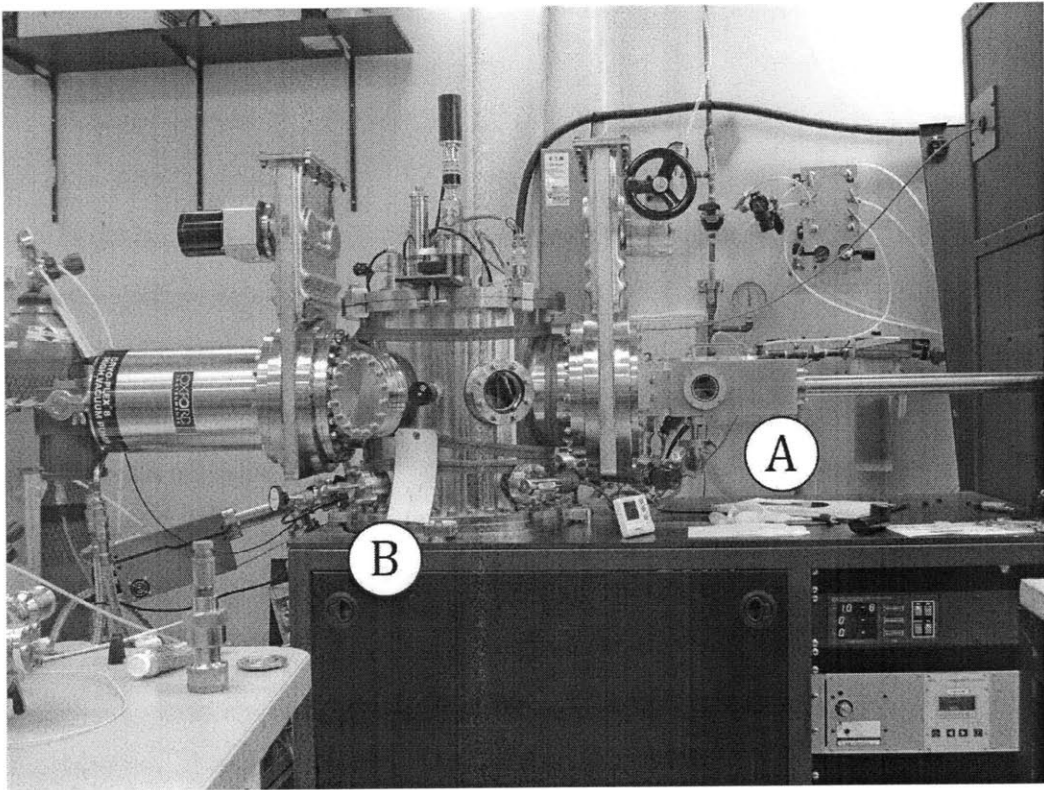
Figure 2-1: The QNN Laboratory's AJA Sputterer. (A) denotes the sputtering system's load-lock entry point. (B) denotes the sputtering chamber, 30 cm in diameter and 40 cm in height.

procedure was omitted because the front surface arrives from the factory epitaxially smooth. We rely on the heat and low pressure of the sputtering deposition chamber to remove any water contamination deposited on the wafer during transport from the cleanroom to the AJA.

The wafer was loaded, frontside-down, into an inconel chuck cover and was screwed into the base of the chuck. The chuck and wafer, now stuck together, were placed into the load lock of the sputtering system. The load-lock turbo was engaged and once its pressure reaches 3×10^{-5} Torr, the main chamber gate wasopened and a magnetic lever arm was used to push the sample into the main chamber and load it onto the main chamber chuck-mount. Once the transfer arm was out of the chamber and the gate was closed, the chuck holding the sample was set to rotate at 50 rpm and the relative height level was adjusted to 47 mm for the remainder of the sputtering procedure. This height setting of 47 mm corresponded to a target-sample distance of 18 cm.

The temperature control was set to 850° C, and after 7-8 min, the chuck and sample reached temperature. We waited an additional 5 min after first reaching 850° C to stabilize the temperature and also allow any outgassing contaminants to dissipate. During this time period the pressure typically remained below 1×10^{-6} Torr. Pressures above this level indicated a leak in the system or large amounts of outgassing contaminants. Ideally, when the wafer had finished outgassing the pressure baseline was in the low 1×10^{-8} Torr range.

Now we were ready to perform the pre-sputtering maintenance. Keeping the argon cylinder regulator closed, we set the argon flow rate into the main chamber to 100 sccm and waited until the flow rate dropped to below 1 sccm, in order to drain any argon or contaminants trapped in the flow line. We then flushed the gas lines by opening the argon cylinder regulator, restoring the 100 sccm flow.

After flushing the lines, we performed a short target cleaning procedure to sputter away the top layer of the niobium target, which may have been contaminated from other users, venting, or slow leaks in the chamber. While cleaning the target, the shutter on the target remained closed, so that any particulates ejected from the contaminated surface of the target would be collected on the inside of the shutter and not spoil the surface of the sample. The power for the sputtering target was sourced from a DC gun at a maximum possible current

14

of 1 A. With the argon flowing at 100 sccm, the DC gun current was set to 30% (300 mA), and the chamber pressure was set at 30 mTorr. The pressure was immediately lowered to 3 mTorr once sparked, and the target plasma was left on to clean for 3 min.

Using the parameters of the last paragraph in the sputtering system, niobium accumulated on the target at 27Å/min, measured by system's built-in quartz oscillator thickness monitor. To achieve the thick (320 nm) niobium we used, the target shutter stayed open for 2 hours, after which the target shutter was closed, the plasma was shut off, and the gas flow was set to zero. For sample cooldown the cryo pump was fully opened to bring the pressure down as much as possible, and the sample was cooled for at least two hours, although typically it remained in the chamber overnight. After sputtering, the substrate was immediately placed into a nitrogen drybox until the next step in processing, to minimize oxidation.

The backside sputtering procedure was identical to the frontside, except that the heating was omitted and the sputtering time was reduced from 2 hours to 5 min, just enough to give a visible layer. Note that the backside sputtering takes place first, since it was important for the even heating of the wafer during frontside deposition.

2.2.1 Photolithography and etching

Once the two niobium layers were deposited, the wafer was ready for processing. To fabricate our resonators, micron-level precision was needed, and so processing was done using an ultraviolet optical lithography setup and reactive ion etching. A schematic showing the layout of the resonator was shown in Figure 2-2. The wafer mask was designed in the GDSII format using the program LayoutEditor[2], and manufactured at Advanced Reproductions Corp.[3] on a 10 cm square soda-lime mask patterned with 1.5 mm chrome. Because the photoresist used was negative, the mask was a negative mask, which means that all the electrodes of the fabricated devices were blank areas on the mask. Correspondingly, gaps on the final resonator had their chromium equivalents on the mask. Once the mask was designed and fabricated, the remainder of the processing was performed in the NSL clean

---

[2]http://www.layouteditor.net/
[3]http://www.advancerepro.com

room. All of the following processes except baking occured at room temperature, which for the NSL clean room was $23\pm1°$ C.
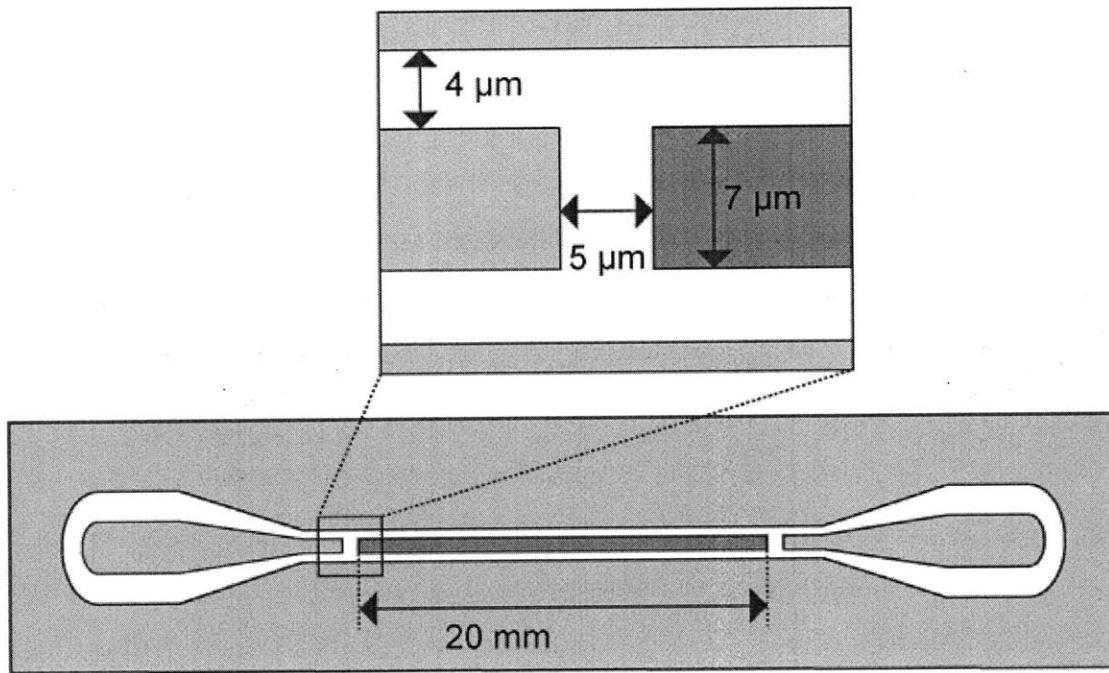
Figure 2-2: Schematic of the resonator showing the contact pads (grey electrodes) and resonating center electrode (red). Not to scale.

We began by spinning NR9-3000P photoresist[4] onto the wafer at 3000 rpm for 40 sec, yielding a resist thickness of approximately three micrometers as seen in SEM images. Next, the wafer was prebaked on a hot plate at $90°$ C for 5 min after which it was moved to the Tamarack exposure system [5]. The Tamarack lamp was turned on and allowed to warm up for 10 min, after which the exposure intensitywas measured. The typical exposure intensity was 3200 μW/cm^2, and at that intensity the resist was exposed for 90 sec, yielding a total exposure of 288 mJ/cm^2. The NR9-3000P SOP suggests much hotter bakes ($150°$ C) than we were using, but we devised this recipe to avoid heating the niobium too much and possibly increasing the thickness of a loss-inducing oxide surface layer. Additionally, the SOP states that only an exposure of 21 mJ/cm^2 was necessary, but early tests revealed the change in bake temperatures also required much longer exposures.

---

[4]From Futurrex http://www.futurrex.com/
[5]Model PRX-200-6 (Hg Lamp), Tamarack Scientific Co.

The mask was manually placed onto the sample, and a vacuum seal was placed around the mask to pump out any air between the resist and the mask and ensure intimate contact. Typically the interference fringes seen in the yellow clean room light were limited to two or three localized bands, indicating some small grains of dust were present on the surface but that intimate contact to within 1-2 μm was achieved over most of the surface. The mask-wafer pair was then moved directly under the Tamarack lamp and was exposed for 90 sec. Following the exposure, the wafer was baked at 90° C, this time for 2 min.

Now the sample was ready for development and etching. The sample was submerged in room-temperature RD6[6] and agitated lightly in the developer for 16 sec after which it was immediately rinsed by placing it under the flow of DI water for 30 sec. After rinsing, the sample was blown dry with nitrogen and taken to the optical microscope for examination[7], the results of which can be seen in Figure 2-3.
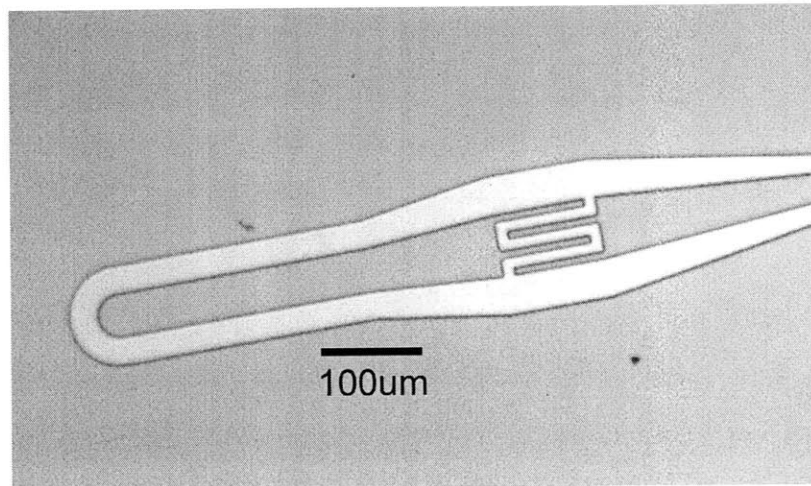
Figure 2-3: Sample amcc010_04 4-finger coupling capacitor, patterned into NR9-3000P resist

If features were not fully developed, the sample was taken back to the chemical bench and developed for 3 more seconds, following the same development procedure as before. The criteria for "fully developed" was only that the smallest feature gaps (in our case, 10μm) were visible in the microscope. Once features were satisfactorily resolved in the resist, the sample was baked one last time at 90° C for 2 min and could then be etched. Etching was

---

[6]From Futurrex http://www.futurrex.com/

[7]It should noted that the microscope must be fitted with a UV filter before examination, lest it further expose the portion of the sample being viewed.

performed in a Plasma Therm 790 series RIE. The process begins by cleaning the chamber for 5 min using the preconfigured "NEWCLEAN" recipe, which scrubs the inside of the chamber with the same set of gases that the etching process used. Afterwards, the sample was placed onto the conductive center of the RIE chamber. The lid was closed, and once the vacuum seal was made the CF_4/O_2 process began. The chamber was reduced to a base pressure of 8×10^{-5} Torr and held at that level for 10 sec. Next, to flush the lines and chamber, a gas mixture flowed for 1 min at 20 mTorr, with a ratio of 1.5 sccm O_2 to 15 sccm CF_4. After the lines were flushed, the plasma was sparked and held at 150 W of RF power and the sample was etched for 24 min. Finally, the chamber was pumped down to 2×10^{-3} Torr, held there for 10 sec, and vented to atmosphere. A low-zoom visual inspection of the surface took place using the Dektak's camera to ensure that the niobium had been fully etched away in the exposed areas. The Dektak camera was used since it zooms in on the sample from a 45°angle while the sample was illuminated from above. This made it easier to spot any thin residual layers of niobium that were not fully etched away.

If niobium remained, a second, shorter round of etching in the RIE took place, using the exact same process outlined above except with 1-2 min of etching time. Otherwise, if the etching was satisfactory, the sample was cleaned of the remaining photoresist by sonicating it in an acetone bath for 5 min. Normally the photoresist could be removed just by submerging it in acetone, but the etching procedure interacts with the resist and the resulting photoresist post-etch was much more difficult to remove, hence the sonication. Lastly, the sample was gently rinsed with acetone, methanol, IPA, and then deionized water in that order, after which it was blown dry with nitrogen. The final result was visible in Figure 2-4.

2.2.2   Gold Contact Pads and liftoff

Although the resonator was fundamentally complete after etching, in order to test it in our probe station we needed to add a gold layer to the surface of the contact pads, so that the probes could make good electrical contact. Initially, we probed the niobium while it was bare. This approach did not work well, because in the cryogenic regime the niobium was very hard, and the probes had a difficult time making contact. Even small vibrations
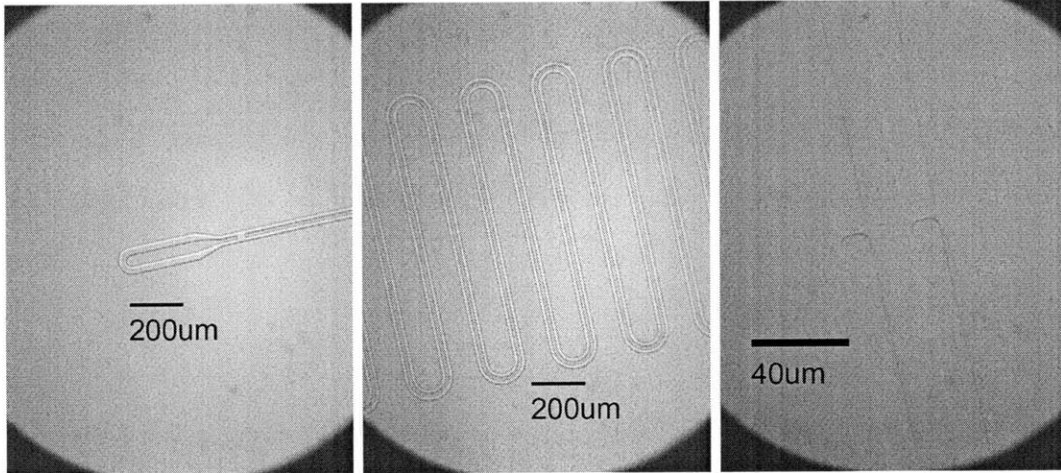
Figure 2-4: Optical microscope images of the etched resonator from sample amcc001_01

would move and disturb the contacted probes enough to ruin transmission measurements. Additionally the unreliable electrical contact made it difficult get consistent results–without gold contact pads, probing and reprobing the same resonator yielded wildly varying (± 10 dB across the entire spectrum) transmission characteristics.

The gold contact pads were added to the device using a liftoff procedure very similar to the etching procedure, since the liftoff resist used–NR9-3000PY–was a variant of the photoresist used in etching, NR9-3000P. First, the gold contact mask was made by editing the device mask in LayoutEditor and sending it to be printed on an emulsion transparency[8] . The transparency had very rough features, with a minimum feature size of 25µm, but since the devicewas already accurately patterned, the gold pattern on top could be very rough.

The resist was spun onto the patterned device at 3000 rpm for 40 sec and then prebaked at 90° C for 2 min. The samples were then wrapped in foil, taken out of the NSL, and brought to the MJ83 broadband UV mask aligner in the Microsystems Technology Laboratory (MTL). At the mask aligner, the transparency mask was taped to a 10 cm glass plate and the pattern was aligned with the resist-coated wafer. Once aligned, hard contact was forced between the mask and wafer, and the combination was exposed with the internal mercury lamp for 2 min. Just as in the etching process, the exposed wafer was then baked at 90° C for 2 min and developed in RD6 for 16 sec. In this case, however, the resistwas

[8]5080 dpi transparency printed from Pageworks, Inc.

not post-baked after development, since SEM examination showed that the NR9-3000PY reflowed if post-baked, changing its sidewall profile from an undercut to a shallow slope inappropriate for liftoff. After development, the wafer was mounted onto a fixture and placed into an evaporator, where the wafer collected 10 nm of titanium (for adhesion) followed by 60 nm of gold. Once the gold was deposited, the wafer was then sonicated in acetone for 5 min to remove the remaining resist and with it, the excess gold. The sonication was not typically necessary for this type of liftoff, but was performed to make absolutely sure no hardened resist was leftover from the etching procedure. It was finally cleaned in acetone, followed by methanol and isopropanol, and then rinsed in dionized water and blown dry with nitrogen. The final result can be seen in Figure 2-5.
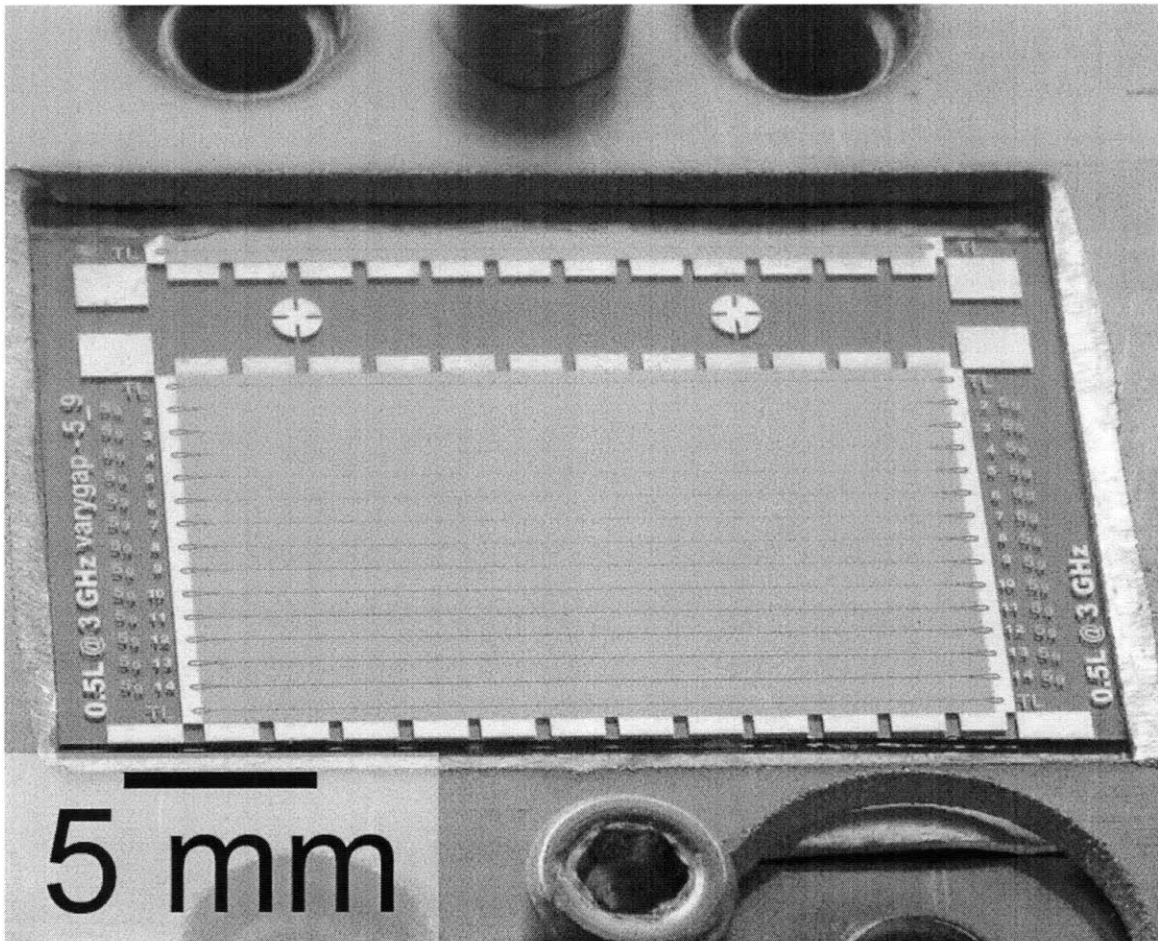
Figure 2-5: The fully fabricated set of straightline resonators mounted in a copper frame

Chapter 3

Theory of Superconducting

Resonators

To accurately understand the measurements we made, we examined the theory behind superconducting resonators. Starting with the basic models of transmission line theory and lumped element resonators, we were able to interpret our results and gain an intuition for how to improve the devices. The following sections set up the theoretical understanding necessary to analyze the results presented in Chapter 6.

3.1 Transmission Line Model

Everything about the resonator can be analyzed using standard transmission line theory. In this section, we break down the resonator first as a transmission line, then further into the constituent parameters of the transmission line's distributed circuit model in order to understand how the physical shape of the device affects its operation.

3.1.1 The Transmission Line as a Circuit Model

Though the parallel RLC circuit gives us an excellent description of the overall circuit parameters and intuition as to what kind of behavior to expect, it paints an incomplete picture. In a transmission line, the phase and magnitude along the length of the resonator can be most fundamentally examined by breaking the system down into a distributed cir-
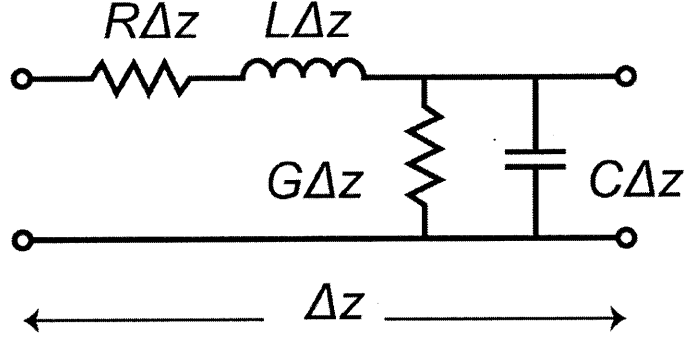
Figure 3-1: Segment Δz of a general two-conductor transmission line represented in its distributed circuit model form.

cuit model, where an infinitesimal length of the TL is represented by the circuit model of Figure 3-1. This formulation is more thoroughly explained in the literature[21]. We will simply note that a uniform lossless transmission line with characteristic impedance Z_0 with propagation constant β has the standard solution

$$V(z) = V_0[e^{-j\beta z} + \Gamma e^{j\beta z}] \tag{3.1}$$

$$I(z) = \frac{V_0}{Z_0}[e^{-j\beta z} - \Gamma e^{j\beta z}], \tag{3.2}$$

where Γ is the voltage reflection coefficient, and $V(z,t) = Re\{V(z)e^{j\omega t}\}$. The device under consideration is most accurately described by an open-circuit half-lambda ($\lambda/2$) resonator, for which $\Gamma = 1$. The input impedance of such a lossless resonator is

$$Z_{\text{in}} = Z_0 \coth(j\beta)l \tag{3.3}$$

The resonant modes occur whenever the length l is a multiple of $\lambda/2$, where $\lambda = 2\pi/\beta$. The resulting voltage distribution $V(z)$ for the first 3 resonant modes is seen in Figure 3-2.

3.1.2 Physical Geometry of the Device

Since the transmission line model is generalized, the device can be designed in any particular geometry and still maintain the fundamental properties of the TL resonator. As long as the
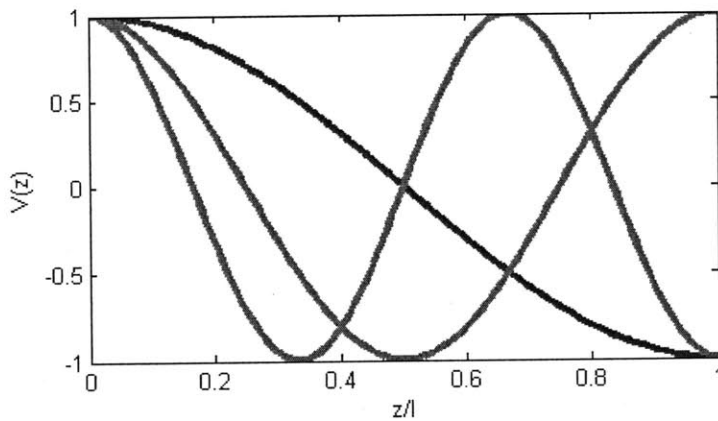
Figure 3-2: First three resonances for an open transmission line of length $l = \lambda/2$
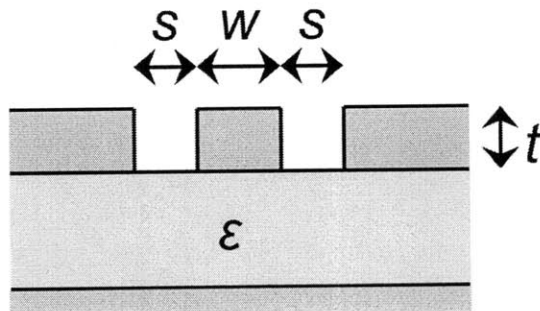
Figure 3-3: Side view of the CPW geometry showing the characteristic parameters width of center signal line w, spacing between signal line and ground s, and thickness of the conductors t.
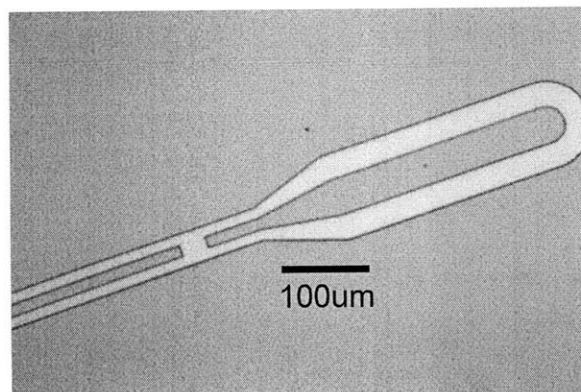
Figure 3-4: Top view of the fabricated CPW line showing the resonator transmission line (left electrode) and input transmission line. The gap is the coupling capacitor.

parameters R, L, G, and C per unit length can be found, the general model is useful. The device addressed in this report has been designed as a grounded coplanar waveguide (CPW) transmission line resonator, as shown from above in Figure 3-4 and whose cross-section can be seen in Figure 3-3. The grounded CPW consists of a thin flat dielectric sandwiched on either side by a conductor, one side of which is etched to form a signal line bounded on either side by ground planes. In our particular case, we chose to use niobium for the conductor and sapphire for the dielectric. The niobium was chosen for its superconducting properties and convenience of fabrication. The sapphire makes an excellent dielectric due to its low loss tangent and high permittivity as discussed in Chapter 2.

With the Nb-sapphire material stack, the conductance G is negligible and can be removed from the transmission line circuit model. However, there is no simple field solution to solve like that which exists for a parallel plate transmission line. Fortunately, previous work[24][8] has been done to find a conformal mapping technique for the CPW that yields the geometric contribution to inductance and capacitance per unit length

$$L_1^m = \frac{\mu_0}{4} \frac{K(k_0')}{K(k_0)} \tag{3.4}$$

$$C_1^m = 4\epsilon_0 \epsilon_{\text{eff}} \frac{K(k_0)}{K(k_0')}. \tag{3.5}$$

In these equations K is the complete elliptic integral of the first kind with the geometric arguments

$$k_0 = \frac{w}{w + 2s} \tag{3.6}$$

$$k_0' = \sqrt{1 - k_0^2}. \tag{3.7}$$

Though these equations only address the CPW, and not the grounded CPW, the sapphire layer in our particular device is far too thick to contribute significantly to the geometric capacitance. Additionally, there is no geometric contribution to the resistivity of the transmission line; the loss induced in the superconductor is purely due to the two-fluid model,

24

and will be taken into account via the surface impedance in a later chapter, as will the kinetic inductance.

3.2   Lumped-Element Model of a Resonator

The simplest model of a resonator comes from its lumped-element representation, which we treat in this section. It provides insight to how the resonator couples with the outside world, in addition to giving basic formulations for Q and ω. In this section, we also introduce the idea of the loaded quality factor Q_L, which is the measurable figure of merit in this thesis, as it includes both the losses intrinsic to the resonator and the losses it experiences through coupling with the outside world.

3.2.1   Quality Factor of a Lumped Element Resonator
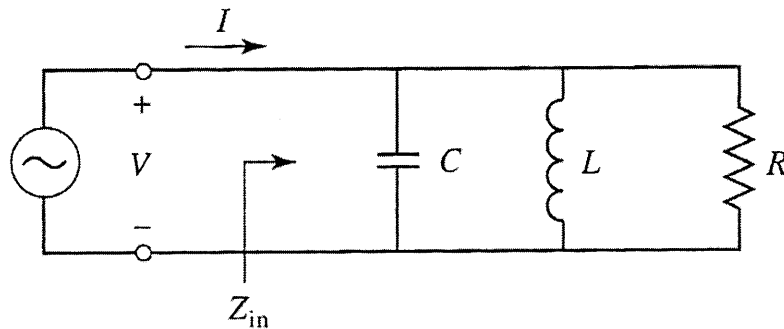
Figure 3-5: Parallel RLC circuit with sunusoidal voltage source.

In order to understand fully the dynamics of the superconducting cavity described in the introduction, first we must address the properties of a basic resonator. In its ideal lumped element form, a resonator can be constructed out of only two elements: an inductor and a capacitor. Energy is traded back and forth between the two components of the system, and a probe at either of the two nodes of the circuit would show that current and voltage vary sinusoidally with time. Such a resonator is lossless, since its ideal components have zero dissipation, but as we will be dealing with a specific device we will skip this treatment and go directly to the relevant circuit: the parallel RLC resonator, as shown in Figure 3-5. The

reason the parallel RLC resonator is appropriate is because the modes supported ($n\lambda/2$) match those of our device input.

By analyzing this form of resonator, we can develop an intuition for how the TL resonator will behave. Nominally, we would like to store as much energy in the cavity as possible to generate a high electric field. The voltage source will apply power to the circuit, which will increase until it reaches an equilibrium wherein the energy dissipated each second is equal to that of the power delivered. To quantify this, it is helpful to define Q, the quality factor as

$$Q = \omega \frac{\text{(average energy stored)}}{\text{(energy loss/second)}}$$

(3.8)

$$= \omega \frac{W_\mathrm{m} + W_\mathrm{e}}{P_\mathrm{loss}}$$

Where W_m and W_e are the stored magnetic energy (in the inductor) and stored electrical energy (in the capacitor), respectively. Since we wish to have high amounts of energy stored in the resonator with low loss, we desire a high quality factor. In order to examine the components of Q more closely, we can look at Z_in, the input impedance of the lumped-element resonator, where

$$Z_\mathrm{in} = \left(\frac{1}{R} + \frac{1}{j\omega L} + j\omega C \right)^{-1},$$

(3.9)

and for a resonator of length l, in terms of the transmission line parameters

$$L = \frac{2L_\mathrm{l} l}{\pi^2}, C = \frac{C_\mathrm{l} l}{2}.$$

(3.10)

Now if we apply a sinusoidal voltage source across the two nodes of the resonator, the complex power of the circuit becomes

$$P_\mathrm{in} = \frac{1}{2} |V|^2 \left(\frac{1}{R} + \frac{1}{j\omega L} - j\omega C \right)$$

(3.11)

and from there it is straightforward to derive the components of Q[21]. In particular,

$$P_{\text{loss}} = \frac{1}{2}\frac{|V|^2}{R} \tag{3.12}$$

$$W_{\text{m}} = \frac{1}{4}|V|^2 C \tag{3.13}$$

and

$$W_{\text{e}} = \frac{1}{4}\frac{|V|^2}{\omega^2 L}, \tag{3.14}$$

finally yielding

$$Q = \omega_0 \frac{2W_{\text{m}}}{P_{\text{loss}}} = \frac{R}{\omega_0 L} = \omega_0 RC, \tag{3.15}$$

where $\omega_0 = 1/\sqrt{LC}$ is the resonant frequency of the system. This formulation of Q shows that for a parallel RLC circuit, the quality factor is directly proportional to R, which is the expected result since for $R \to \infty$ the circuit becomes an ideal LC circuit with no dissipative element and $Q \to \infty$. It is also important to note that this quality factor only describes a resonant circuit completely disconnected from the outside world–that is, when there is no load on it. When the circuit is "loaded" with non-ideal external circuitry, invariably the overall quality factor will lower due to extra loss in the loading components. This can be seen in the relation for the loaded Q, expressed as

$$\frac{1}{Q_{\text{L}}} = \frac{1}{Q_{\text{ext}}} + \frac{1}{Q_{\text{int}}}. \tag{3.16}$$

3.2.2 Coupling to the Resonator
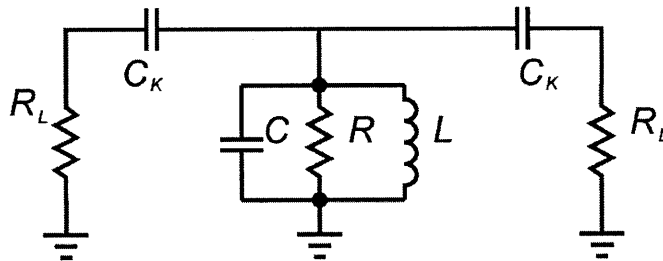
Figure 3-6: Parallel RLC circuit with input coupling circuit (C_κ, R_{L})
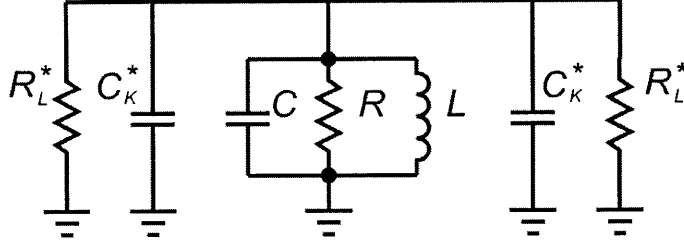
Figure 3-7: The same parallel RLC circuit with norton equivalent input coupling (C^*, R^*)

In order to perform measurements on a resonator circuit, we must somehow couple our measurement input and output to the device. In the case of the device we are examining, this coupling can be described by a pair of input capacitors attached to ground by load resistors as shown in Figure 3-6. Though only a single resistor and capacitor have been added to each side, there is no longer a trivial way to extract the quality factor of the loaded system. Fortunately, Goppl et al. have broken the problem down into a much simpler system that has shown good agreement with experimental results for device geometries similar to the one described in this report[9]. By performing a Norton equivalency of the coupling, the series resistor R_{L} and capacitor C_κ can be equivalently viewed as a parallel capacitor C^* and R^* as seen in Figure 3-7, specifically

$$R^* = \frac{1 + \omega_n^2 C_\kappa^2 R_{\mathrm{L}}^2}{\omega_n^2 C_\kappa^2 R_{\mathrm{L}}} \tag{3.17}$$

$$C^* = \frac{C_\kappa}{1 + \omega_n^2 C_\kappa^2 R_{\mathrm{L}}^2} \tag{3.18}$$

where $\omega_n = n\omega_0 = 1/\sqrt{L_n C}$ is the angular frequency of the nth mode of resonance. Now, by summing the parallel capacitors and parallel resistors, the circuit can be reformulated as a single RLC parallel resonator whose quality factor represents that of the loaded system, Q_{L}.

$$Q_{\mathrm{L}} = \omega_n^* \frac{C + 2C^*}{1/R + 2/R^*} \approx \omega_n^* \frac{C}{1/R + 2/R^*} \tag{3.19}$$

Note that C^* can be neglected in the numerator only because of the particular coupling setup used in this device (i.e. for our device $C^* \ll C$). In addition to approximating Q_{L}, this

model shows that increasing the coupling capacitance decreases the resonance frequency, because

$$\omega_n^* = \frac{1}{\sqrt{L_n(C + 2C^*)}}. \tag{3.20}$$

Now it is possible to derive the relationship between the total quality factor Q_L, the intrinsic quality factor Q_{int}, and the external quality factor Q_{ext}. In the literature[21], we see that for a parallel resonant circuit attached to a single external load resistor R_L, the external quality factor can be shown to be $Q_{ext} = R_L/(\omega_0 L)$. By interpreting our external coupling circuitry as a single resistor (remember that $C + 2C^* \approx C$ so we can neglect the external capacitors) the corresponding load resistor becomes $R_L = R^*/2$, and we come to the conclusion that

$$Q_{int} = \omega_n RC, \text{and} \tag{3.21}$$

$$Q_{ext} = \frac{\omega_n R^* C}{2} \tag{3.22}$$

Thus there are two regimes of Q_L in which the coupled oscillator operates, the over-coupled and undercoupled. In the former, $Q_{ext} \ll Q_{int}$ and the loaded quality factor is governed by Q_{ext} and so can be well-approximated by $Q_L \approx C/2\omega_n R_L C^2$, or more simply the loaded quality factor is dominated by the coupling capacitance $Q_L \propto C_\kappa^{-2}$. However, at very small coupling capacitances $Q_{int} \ll Q_{ext}$, the undercoupled regime dominates, and Q_L saturates as can be seen in Figure 3-8. One interpretation of these two regimes is that in the overcoupled scenario, most of the energy the cavity loses is being sent out to the apparatus that connects to it. In the undercoupled scenario, the energy loss is dominated by dissipation intrinsic to the resonator, such as radiation or dielectric losses. Experimentally, this means that by continually lowering the coupling capacitance, once we observe the loaded quality factor saturating, the Q_{ext} term has becomes negligible and Q_{int}–a parameter which is intrinsic to the resonator and which need only be found once–is determined. Additionally, a direct relationship is formed between the Q_L and our original coupling capacitance, C_κ by Eq. (3.16), (3.17), and (3.22) and so by either simulating C_κ or measuring Q_L, the other

parameter may be determined.
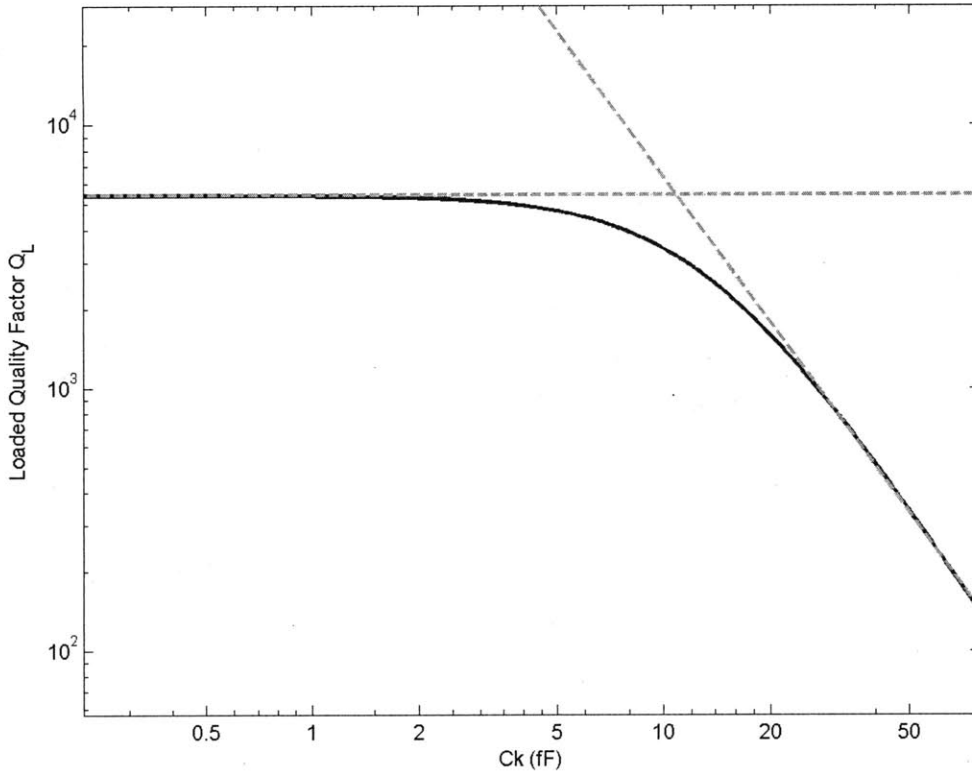
Figure 3-8: Input coupling versus quality factor in $\lambda/2$ resonator. Blue line shows the theoretical relationship between coupling capacitance and quality factor. Green dashed lines are over (sloped line) and undercoupled (horizontal line) regimes

3.3   The Superconducting Resonator

Up until this point we have treated the resonator conductors as though they were purely classical, ignoring the effects of superconductivity. In this section we explore the effects that superconductivity adds to our model–namely kinetic inductance. We also introduce the concept of surface impedance, and examine the temperature dependence of Q in the superconducting regime.

3.3.1 Taking Superconductivity into Account

Having accounted for factors that affect the resonator when viewed as normal metal, we now examine the influences on the system that superconductivity will have on the circuit parameters. (For simplicity, we assume that there is zero magnetic field penetrating the device when it is brought below the superconducting transition temperature T_c). We can begin by modeling the superconductor as a lossless conductor and drop the R_l term from the transmission line model. However, that would neglect the implications of the penetration depth λ of the superconductor and its interaction with the two-fluid model of superconductivity. The magnetic field penetration into the surface of the niobium excites both the Cooper pairs in the superconducting channel and the unpaired electrons in the normal channel. There are two consequences of the two-fluid model that affect the superconducting transmission line model. First, a kinetic inductance term L_{ki} must be added to the existing geometric inductance to account for the 'inertial' movement of the oscillating Cooper pairs in the superconducting channel so that

$$L_l = L_l^{\mathrm{m}} + L_l^{\mathrm{ki}}. \tag{3.23}$$

Secondly, the resistive term R_l must be reinstated to account for losses incurred by scattering in the normal channel. Since both terms rely on the two-fluid model, they will depend fundamentally on the ratio of Cooper pairs to unpaired electrons, which in turn is determined by the ratio T/T_c. While it may seem that these terms should be found empirically by varying the temperature (they can be), we can instead relate them to the surface impedance Z_s of the superconductor.

3.3.2 The surface impedance of a superconductor

Due to the magnetic penetration into the surface, a superconductor can be thought of as a perfect conductor with a surface impedance

$$Z_s = R_s + j\omega L_s. \tag{3.24}$$

For simple transmission lines such as the parallel-plate TL, and for specific types of geometry and material combinations (such as thick Al[15]) complete analytical solutions exist for Z_s. However, for the general case of a CPW made of arbitrary materials, the governing equations are extremely complex integrals and must be solved numerically. To give an idea of the involvement of the solutions at low enough temperatures or at high enough frequencies, Ohm's law becomes non-local[6]. What this means is that the current density $\vec{J}$ at a point $\vec{r}$ is not only directly affected by the electric field at that point, but is also influenced by a complex weighted average of $\vec{E}$ in a volume around $\vec{r}$. The full electrodynamic analysis is available in Gao[8], but we will presently skip the (lengthy) details and instead focus on the effects.

We have coded a numerical solver for the surface impedance equations based on the Mattis-Bardeen kernel formulation originating in Popel[20], and, using only material parameters, are able to determine Z_s based the independent variables of ω and T. The code may be viewed in Appendix B. The parameters required are the London penetration depth λ_{L0} at zero temperature, T_c, the mean free path l_{mfp}, and two of the following three parameters: the coherence length ξ_0, Fermi velocity ν_0, and zero-temperature binding energy Δ_0 since they are directly related by

$$\xi_0 = \frac{\hbar\nu_0}{\pi\Delta_0}.$$

(3.25)

These parameters for Nb[20] are listed in Table 3.3.2 for reference.

Table 3.3.2: Parameters for bulk Nb

T_c [K]	9.2
λ_{L0} [nm]	33.3
ν_0 [10^6 m/s]	0.28
ξ_0 [nm]	39
l_{mfp} [nm]	20
Δ_0 [meV]	1.395

Once we have the material-dependent surface impedance, it is possible to determine the

contribution of L_{ki} to the total resonator inductance L because they are linearly related by a geometric factor g[15]. Specifically,

$$L_{\mathrm{ki}} = gL_{\mathrm{s}}. \tag{3.26}$$

While normally requiring a numerical solution of a contour integral, in the case of $t \ll w$ (such as our CPW is) the calculation for g has been derived by Collin[7] and is estimated to be accurate to within 10% for $t < 0.025w$ and $k < 0.8$. This approximation for g is

$$
\begin{aligned}
g &= g_{\mathrm{ctr}} + g_{\mathrm{gnd}} \\
g_{\mathrm{ctr}} &= \frac{1}{4aK^2(k)(1-k^2)} \left[\pi + \log\frac{4\pi a}{t} - k\log\frac{1+k}{1-k} \right] \\
g_{\mathrm{gnd}} &= \frac{k}{4aK^2(k)(1-k^2)} \left[\pi + \ln\frac{4\pi b}{t} - \frac{1}{k}\ln\frac{1+k}{1-k} \right],
\end{aligned}
\tag{3.27}
$$

where $k = a/b$.

Now that we can calculate g, we can take the correct proportion of L_{s} and finally arrive at L_{ki}. In addition, we can now calculate another useful parameter, the ratio of kinetic inductance to total inductance

$$\alpha = \frac{gL_{\mathrm{s}}}{L_{\mathrm{m}} + gL_{\mathrm{s}}}. \tag{3.28}$$

This parameter describes how sensitive factors that rely on the circuit's inductance–particularly the quality factor and the resonance frequency–will be to variables that affect the kinetic inductance, most notably the temperature.

The calculation of α can be verified by comparing the experimental data of the under-coupled Q_{L} (effectively Q_{int}) with the quality factor computed from the numerical surface impedance for a range of temperatures below T_{c}. Since the Q and ω of a parallel RLC circuit can be written as $Q = R/\omega L$, we can write an equation for $Q(T)$ and then fit it to the experimental data at different temperatures with two parameters: α, and a limiting quality factor of $Q(0)$ that represents the baseline power leakage of the device at zero temperature[15]. It takes the form

33
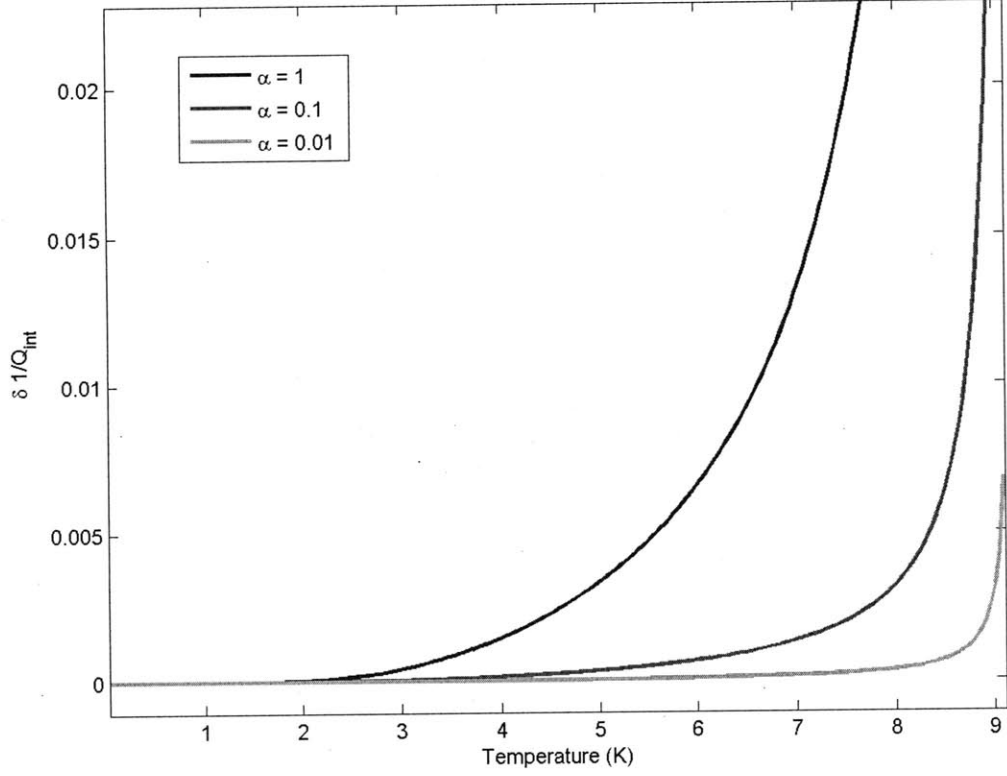
Figure 3-9: Change in the inverse quality factor versus temperature

$$\frac{1}{Q(T)} = \frac{1}{Q(0)} + \frac{\omega_0 L_s(T)}{\alpha R_s(T)}. \tag{3.29}$$

. Similarly for the shift in resonant frequency,

$$\frac{\delta\omega_0}{\omega_0} = \frac{\omega_0(T) - \omega_0(0)}{\omega_0(0)} = -\frac{\alpha}{2}\frac{L_s(T) - L_s(0)}{L_s(0)}. \tag{3.30}$$

One such plot derived from our surface impedance numerical solver is shown in Figure 3-9. This figure shows how the dependence of the quality factor on temperature decreases as the temperature approaches zero. Additionally, the higher the kinetic inductance fraction the more affected the quality factor is by temperature.

3.4 Simulation Based on Z_s

With access to a numerical solution of the surface impedance, a straightforward next step that does not require the use of simulation software is to use the ABCD method to analyze the resonator. Using this formulation, it is possible to gain an understanding of the current and voltage fields in any two-port transmission line.

3.4.1 The ABCD Matrix

The transmission (ABCD) matrix is a simple method by which to calculate the overall impedance properties of circuit networks, or in our case, non-uniform transmission lines. Taking a section of a transmission line Δz long, consider the set of conductors on either edge a "port" It is then clear from Figure 3-1 that our section of transmission line can be thought of as a two-port network. Using the ABCD method, the voltage and current of one end can then be related to the those of the other end by a matrix of four elements in the form

$$
\begin{bmatrix} V_1 \\ I_1 \end{bmatrix} = \begin{bmatrix} A & B \\ C & D \end{bmatrix} \begin{bmatrix} V_2 \\ I_2 \end{bmatrix}
\tag{3.31}
$$

where the elements A, B, C, and D can be calculated from the circuit model Figure 3-1. The result is a straightforward set of equations that concretely relate the two sides of a section of transmission line, and can be cascaded through multiple sections. Assuming a uniform transmission line, in the limit of $\Delta z \to 0$ the original impedance of the line would be retrieved from the cascaded matrix, along with the voltage and current characteristics at any point. There is a limiting factor that the transmission line cannot branch in this simple two-port formulation, but the advantage lies in the simplicity of the formulation.

3.4.2 Sample Application for ABCD Superconductor Simulation

One application of the ABCD method is to use a superconducting resonator as a location-dependent temperature sensor in a cryogenic environment. As can be seen in Figure 3-10, in a $\lambda/2$ capacitatively-coupled resonator such as ours, in its first resonant mode the current
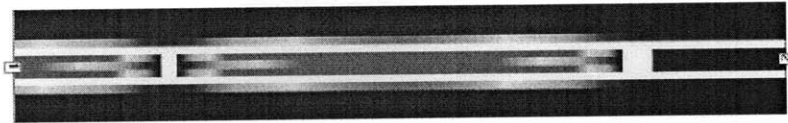
Figure 3-10: Simulation of current density at the first resonant frequency of a capacitatively-coupled $\lambda/2$ resonator

is most excited in the TL's center (the node of V–and therefore antinode of I–in Figure 3-2). At this point, the inductance and resistance is maximally related to the temperature–a warmer temperature with a ratio of T/T_{c} closer to unity will have fewer Cooper pairs providing kinetic inductance, and more unpaired electrons producing scattering and loss. If the resonator were bent into a U shape, the center portion at the bottom of the U could be used as a geometrically static temperature probe. Though it is intuitive that the resonator's impedance–and therefore resonant frequency and quality factor–would change, it is not obvious how to quantify that change. It could, however, be simulated using the ABCD method. To do so, one could model a smooth temperature change over the length of the resonator and include those variable values in the surface impedance calculation for each subsection of the transmission line.

Chapter 4

Early Microwave Tests and Simulation

Up until this point we have explored the physical processes by which we fabricated the resonators, and gained a theoretical understanding of their behavior. In this chapter, we examine some of the early steps undertaken at the beginning of the project. Before building microresonators, we first fabricated and characterized PCB resonators for insight. We also performed simulation on these resonators which gave us a good understanding of how the fields of the resonators worked.

4.1 PCB Resonators

In order to confirm our understanding of how the transmission-line resonators functioned, we designed a set of 5×10 cm resonators and had them patterned in copper on PCB for testing at room temperature. We designed nine resonators in total, with varying coupling capacitances, meanders, and overall lengths. In the end, one of the designs was of particular interest to us: a short straightline (no meander) resonator with plated vias, designed to have its first resonance at 6 GHz. It is shown in Figure 4-1

We had the resonators fabricated on 0.76 mm Rogers 4350B[1], a material which is designed for microwave applications and has a dielectric constant of 3.48. Both the patterned

---

[1]From Hughes Circuits

37
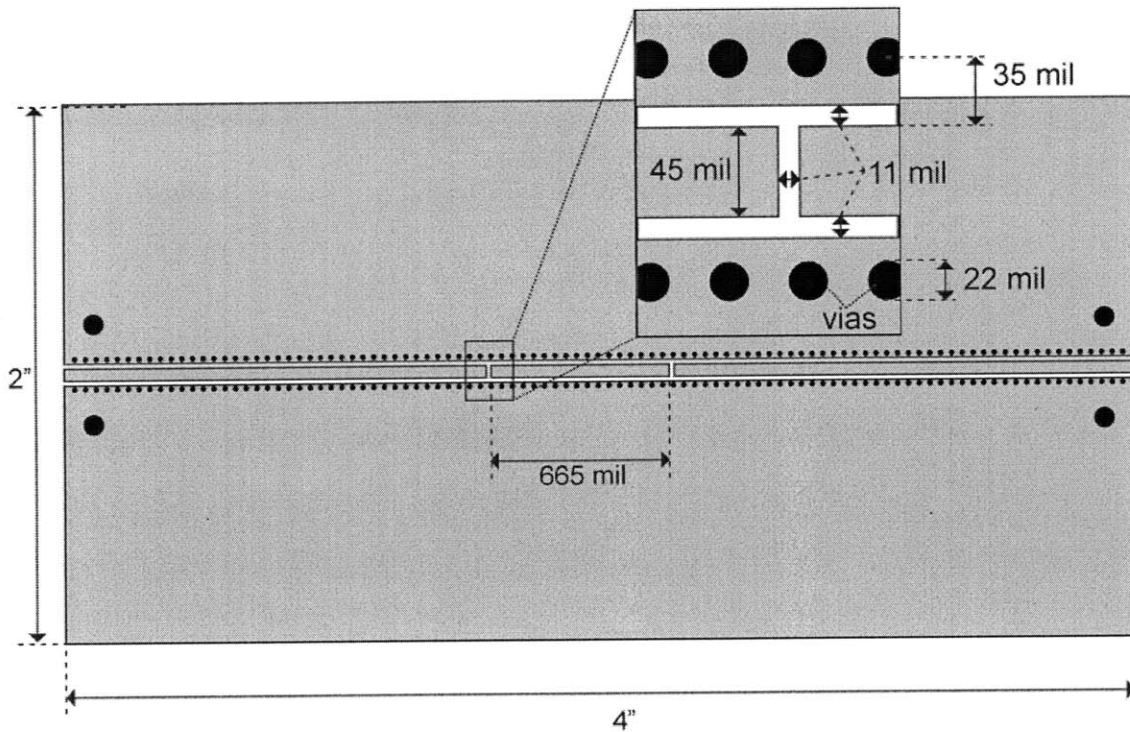
Figure 4-1: PCB resonator schematic drawing

layer on top and the bottom ground layer were "2 oz" copper, or 71 μm thick. The resonators were characterized by the HP 8722C network analyzer (detailed in chapter 5), which connected to the resonators by means of DC-50 GHz end-launch connectors. The vias were drilled into the resonator board and plated with copper on the recommendation of the end-launch manufacturer, Southwest Microwave. They stated that the lateral walls formed by the vias on either side of the strip transmission line acted to prevent additional waveguide modes from being excited; the vias created what is called a "channelized coplanar waveguide" structure.

On testing, we saw a first resonance at 5.39 GHz and a second resonance at 10.75 GHz, well off from the expected 6 and 12 GHz, but reasonable if the dielectric constants used were inaccurate. The quality factor values were 98.5 and 102.1 for the first and second resonances respectively. At this point we needed a method to determine if our results were accurate. We decided to use microwave simulation software HFSS[2] and Sonnet to model the PCB resonator and see if matched our experimental values.

---

[2]By Ansoft corporation

38

4.2 Simulating the PCB Resonators

Once we had the fundamentals of the general resonator geometry and testing done, we began the task of trying to reproduce the acquired data in simulation software. We used two commercial microwave simulation tools, HFSS and Sonnet. Both operate using the finite-element method and so are incapable of reproducing transient phenomenon, but that functionality was not important for our applications because we were focused on the steady-state phenomena of the resonators.

Though the two programs use the same fundamental technique for solving fields, they differ greatly in that HFSS is by default a 3D structural simulator, and Sonnet works by "stacking" 2D layers upon one another. In the end, we chose to use primarily HFSS because there was no good analog for building plated vias between layers in Sonnet to create the channelized CPW. In HFSS, however, we were able to define an artificial perfect electric conductor boundary that would function much the same way as the the plated walls of the via would.

4.2.1 Building the resonator model

The model for the resonator was straightforward to build in HFSS, since the software comes with a set of predefined dielectrics and conductors. We exported the layers from the original design then extruded them to the appropriate thicknesses to recreate the device in 3D. A zoomed-out view of the model is shown in Figure 4-2. However, defining the excitation for the resonator was not so simple. Initially we excited the device using a wave port, a 2D rectangle that imitates the end of an infinitely long rectangular transmission line. Later tests revealed, however, that changing the size and aspect ratio of this wave port altered the resulting scattering parameter profile significantly, as can be seen in Figure 4-3. The overarching result was that any profile could have been fit by altering the shape of the rectangular wave port; there was no sensible pattern of convergence.

To address the variability, we found that using a "lumped port" excitation gave a much more consistent frequency profile. The HFSS documentation also mentions that the lumped port is more accurate when either trying to create a local excitation on the PCB, or making
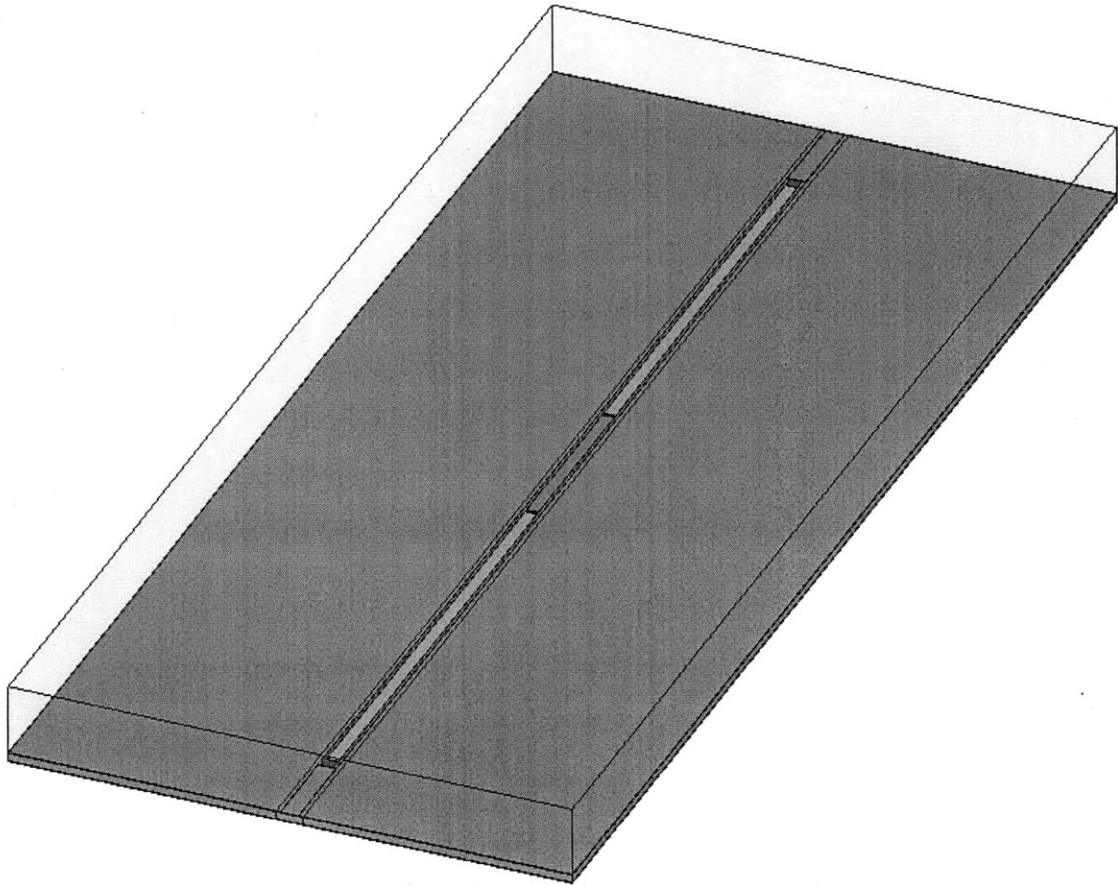
Figure 4-2: HFSS model of PCB resonator
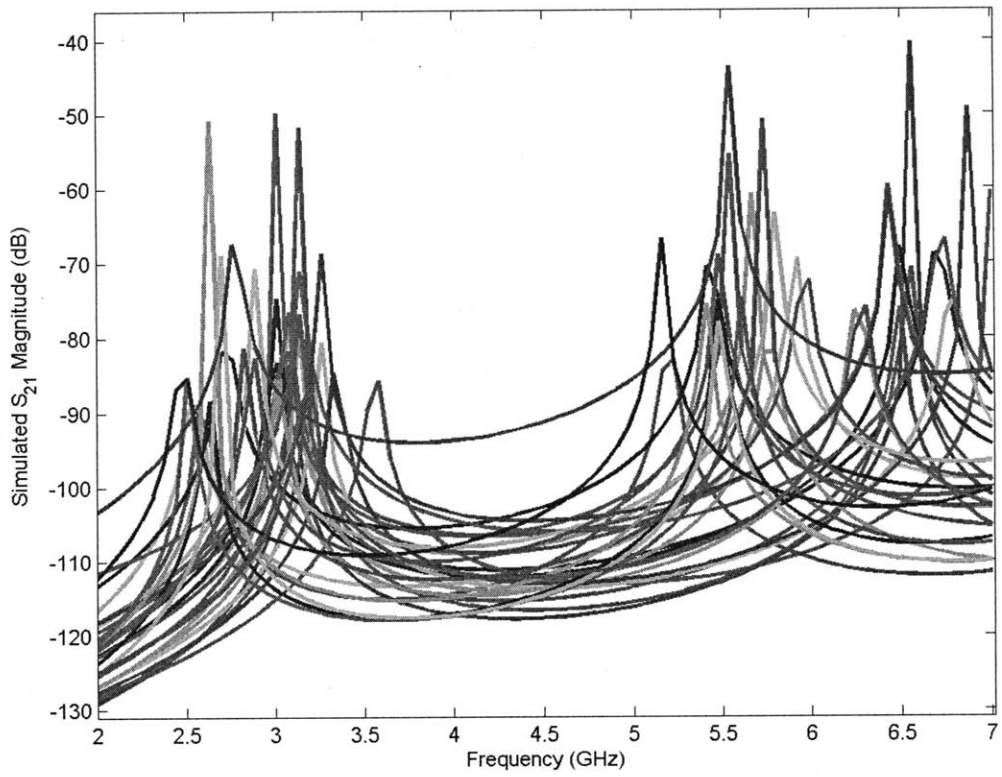
Figure 4-3: Transmission spectra for a resonator with varying waveport sizes

electrical contact to the device with a ground-signal-ground probe, which is how the end-launch connectors functioned. Had we instead modeled the complete system, including the end-launch connectors, the wave port would have been more appropriate. The edges of the 2D wave port sheet function as a reference ground, which can be aligned with the coax shield, and the inner area would excite the center conductor.

While the wave port excites the line as a waveguide, the lumped port acts as an excitation bridge between the ground plane of the resonator and the center electrode. Additionally, instead of defining a shape and allowing the program to calculate the entrance impedance–such as is the case with a wave port–the impedance must be predetermined. We set this impedance value to 50 Ω and placed the lumped port between the ground plane and the input and output transmission lines, as shown in Figure 4-4.
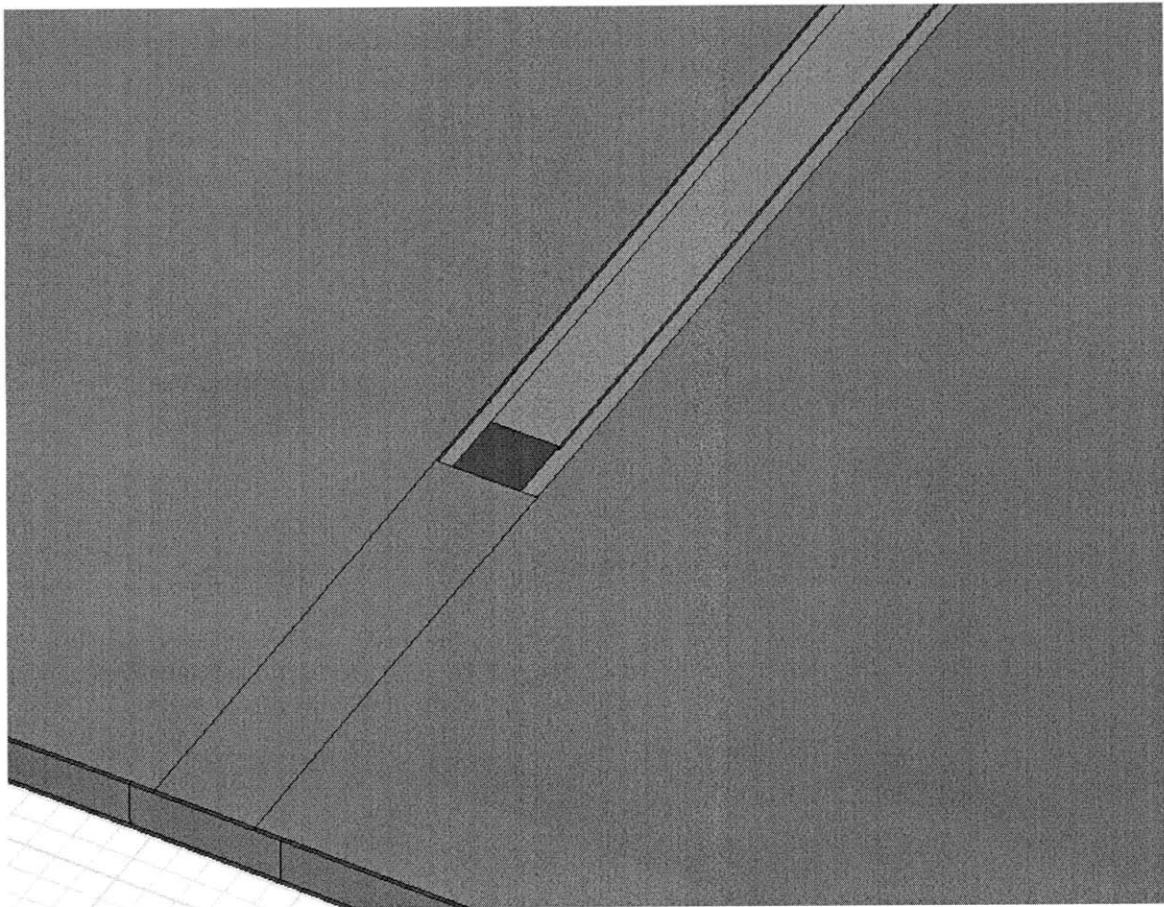

Figure 4-4: Closeup of the the lumped port excitation sheet within HFSS.

Due to the nature of the meshing in HFSS, we also defined an "airbox" around the model

so that it would solve for the field above the resonator. The airbox extended at least $\lambda/4$ in every direction from the center electrode, and all of its faces (save the one coinciding with the dielectric) were made into radiation boundaries, in order to minimize any reflections stemming from the mesh ending abruptly.

4.3 Comparison of Simulation to Experimental Results

Once we implemented the lumped port in our HFSS model, the results of the simulation matched the PCB resonator extremely well. A comparison between the experimental and simulated data is shown in Figure 4-5 . The resonances are clearly visible in the simulation, their frequencies matching the experimental data to within 10% and their quality factors to within 5%. The remainder of the spectrum away from resonance in both cases is -20 dB lower than the resonant peaks, or less than 1% of the maximum output power.
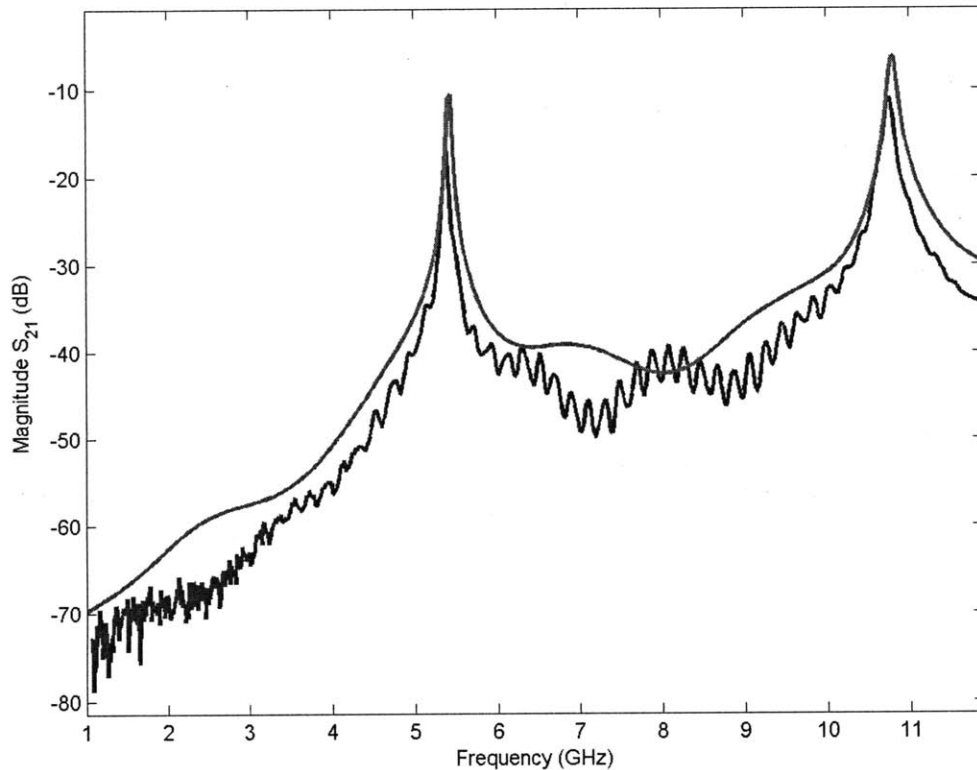
Figure 4-5: Comparison of measurement (blue) and simulation (red) of the PCB resonator.

4.3.1 Simulation field distribution

With the simulation confirming our experimental results, the next step was to examine the microwave field distribution at resonance. We looked at two slices through intersecting the symmetrical origin of the resonator: one perpendicular, and one parallel with the center of the resonator electrode. As can be seen in Figure 4-6, when exciting the resonator into its second resonance, the parallel slice shows the sinusoidal variation in magnitude one would expect in the electric field. The anti-nodes are clearly visible in the center and at either coupling capacitor, forming one period of a cosine, just as transmission line theory would suggest.
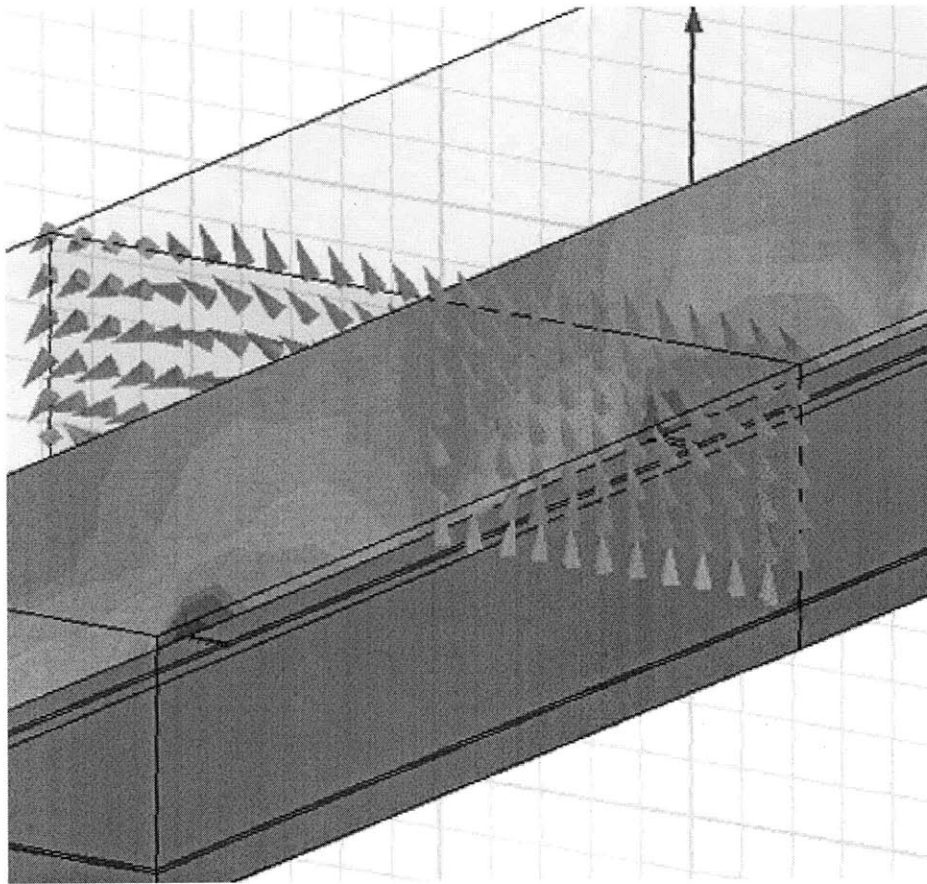

Figure 4-6: PCB electric field plotted in HFSS at second resonance

In the perpendicular slice, the symmetry of the system produces a weak z-directed field in the center, and higher fields along the shorter distance to ground: between the electrodes of the top layer of the PCB. Since the Rogers dielectric below the CPW is 0.76 mm thick,

the majority of the field–and hence the energy in the mode–is carried between the coplanar ground and electrode, which are only 0.28 mm apart.

4.4 Simulating the Niobium Microresonators

Once the PCB resonators had been simulated, the next step was to adapt the geometry of the model to fit that of the actual superconducting resonators we fabricated. Although at the time we were fabricating meandered resonators, the curves of the electrodes greatly increased the amount of mesh points in the model. Instead, we opted to simulate the straight-line resonator to reduce the amount of time and memory necessary to run the simulation. This also simplified the visual inspection of the electric field once the simulation was complete.

4.4.1 Adapting the PCB model

We created the microresonator model in the same way as that of the PCB resonator, only changing geometric values, materials, and removing the perfect electric boundaries since there was no equivalent to the PCB vias in the sapphire-niobium fabrication. Unlike the PCB resonator, the channelization of the niobium microresonator CPW was unecessary because the sapphire dielectric was so thick compared to the resonator gap spacing that no unwanted waveguide mode existed in the frequency range of interest. The dielectric was changed from PCB material to sapphire, with a dielectric constant of 11.5 corresponding to the C axis of the sapphire. Additionally, the conductor was changed to a lossless perfect conductor. By just using the perfect conductor, this model neglected to include kinetic inductance of the surface impedance for the sake of simplification. However, because the 320 nm niobium layer is many times thicker than the London penetration depth of 47 ± 5 nm[14], the kinetic inductance contribution to the overall inductance is small.

The primary challenge with simulating the microresonators was refining the mesh while remaining under memory limits of the modeling computer. It was particularly difficult because of the large difference in length scales between features: the length of the entire device is over 20 mm, but the smallest feature size (the gap capacitors) was 5 µm. The

HFSS meshing process puts more mesh points around areas of fine detail, but the four orders of magnitude difference between our length scales caused it problems. We had to define a mesh refinement box localized above and around the resonating electrode that forced fine meshing, in order to get the scattering parameters to converge. The results for the field just above the resonator electrode and gaps at second resonance can be seen in Figure 4-7.
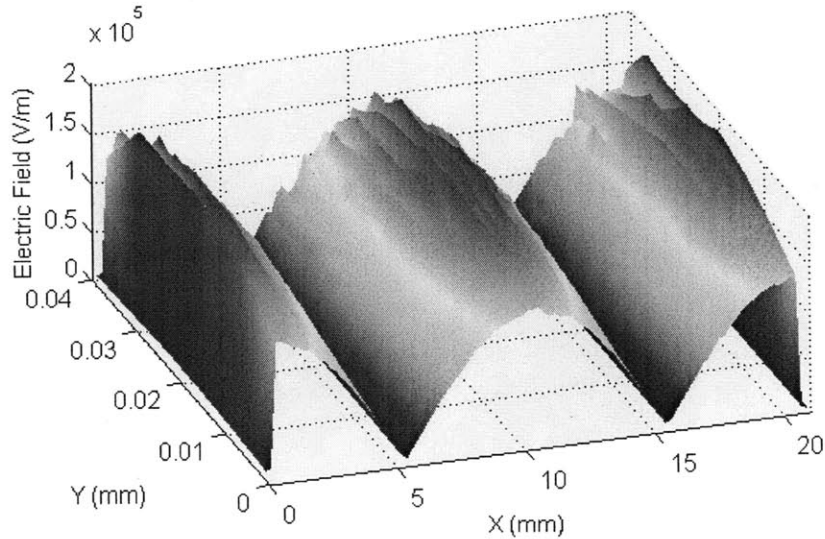

Figure 4-7: Magnitude of the electric field versus XY position at second resonance.

Additionally, we plotted the field dependence along the Z direction. As seen in Figure 4-8 the field falls off exponentially with distance from the resonating electrode. This matched our expectations, and served as a sanity check for the model.

4.4.2 Simulating the coupling capacitances

In order to compare how the physical devices acted with the lumped-element model, we first needed to simulate the coupling capacitances for each resonator. Each coupling capacitor was simulated in HFSS by modeling the geometry as shown in Figure 4-9, from 1 to 10 GHz. Since the electrode material was selected to be a perfect electric conductor, the admittance was completely imaginary and capacitive: $Y_{21} = j\omega C_\kappa$. The resulting admittance values Y_{21} were then used to find the capacitance at any frequency.
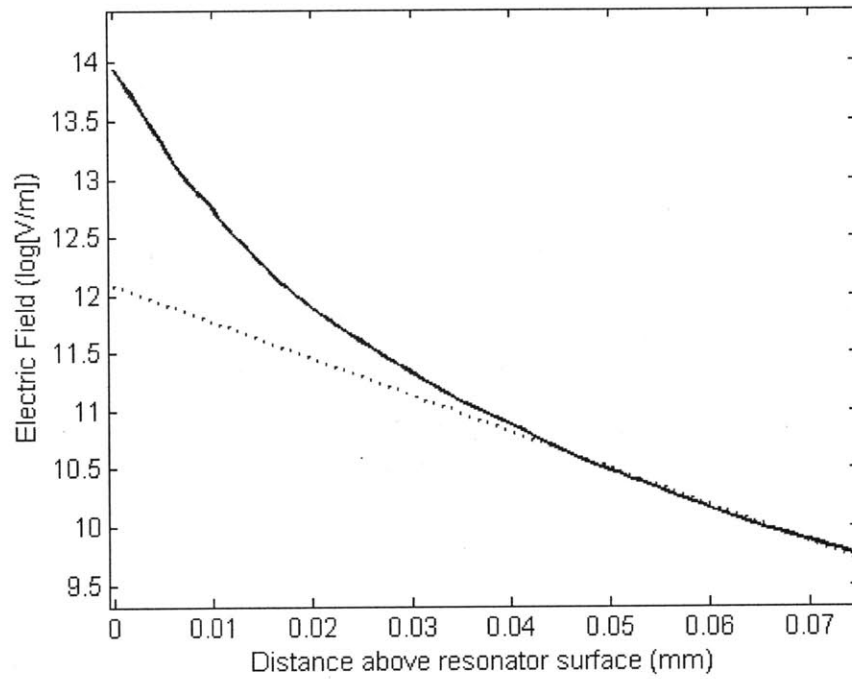
Figure 4-8: Log magnitude of the electric field versus distance from middle of the resonator electrode at its second resonance. Note that as the field gets further from the near-field effects of the electrodes it converges to an exponential falloff as expected
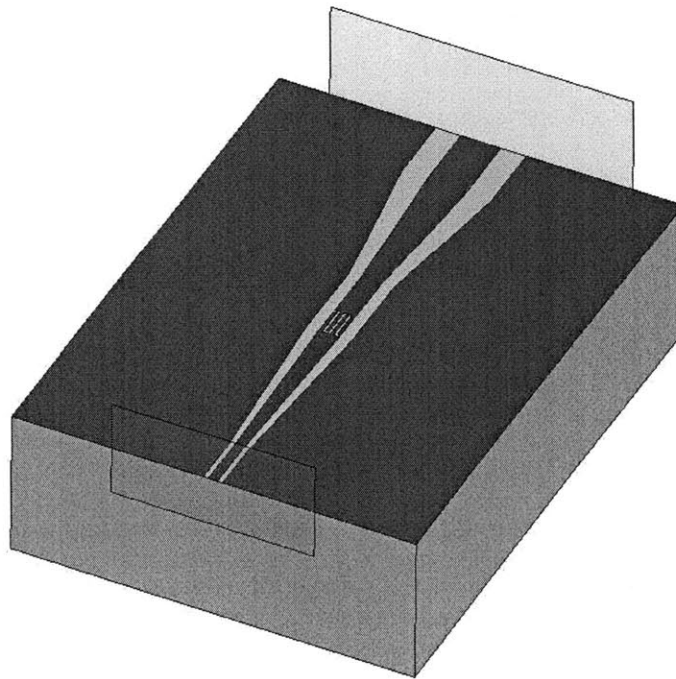
Figure 4-9: Coupling capacitor modeled in HFSS

4.4.3 Including kinetic inductance in the model

The next step for the simulation model is including the kinetic inductance portion to produce more accurate results. This can be accomplished through the judicious use of surface impedance along the faces of the box that define the resonator center electrode. The surface impedance will be in the form of a resistance plus a reactance[28][20], and can be calculated from material parameters as is addressed in section 3.3.2.

Chapter 5

Testing and Characterizing the Superconducting Resonators

In this chapter we describe the testing procedures used when characterizing the superconducting resonators. We used two sets of testing equipment: we found niobium material parameters using a dipstick with a four-point probe, and the we characterized the resonators with a cryogenic probe station. We also detail the microwave and readout electronics used in conjunction with the probe station.

5.1 Dipstick Material Measurements

In the following, we describe the procedure we used to determine T_c for our niobium. Additionally, we describe the method by which the dipstick testing apparatus can determine the residual resistance ratio and sheet resistance for our niobium film. Though these latter tests were never executed to conclusion, they will be in the future and so appear here for reference.

5.1.1 Measurement of T_c

In order to characterize the superconducting properties of the material stack, we ran a four-point measurement on unpatterned samples as they cooled to liquid helium temperatures. The sample was mounted to the end of a dipstick, which was then submerged in a helium

bath inside of a dewar. Four evenly spaced gold spring pins, arranged in a line, pressed against the niobium layer, and current was passed between the outer two pins, as shown in Figure 5-1. This method had the advantage of removing any input resistances from the measurement[26], depicted as resistors in Figure 5-1. While the sample cooled from 297K to 4.2K, a measurement of the voltage between the two inner pins was recorded continuously, and the resistivity of the sample could be calculated by factoring in the relative pin distance.
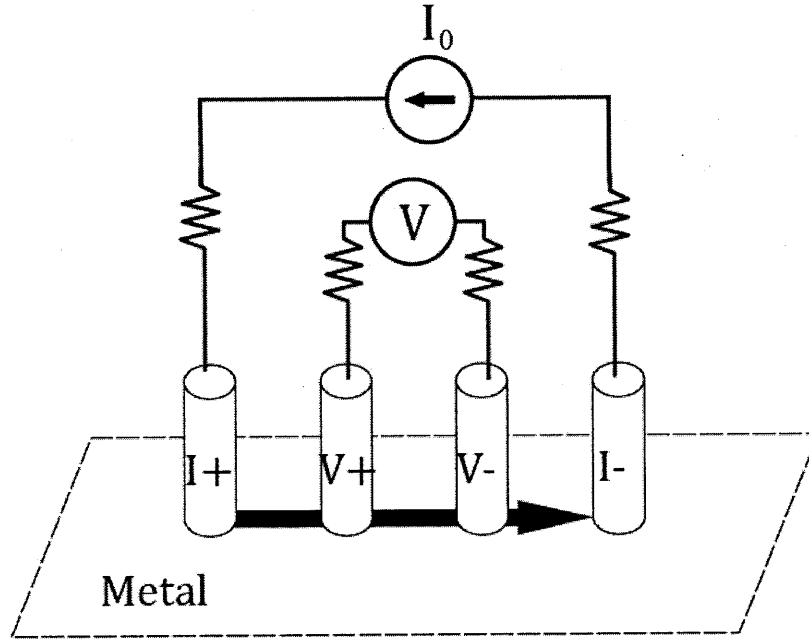
Figure 5-1: Four point measurement depicting current flow, measurement voltmeter, and pin alignment

The general form for the resistivity derived from the four-point measurement is

$$\rho = G \frac{V}{I} \tag{5.1}$$

where G is a correction factor dependent on sample shape, dimensions, and the arrangement of the four electrical contacts. With the dipstick, we were measuring an extremely thin conductor with the four electrical contacts–spring pins–in a line, and the thickness of the niobium, t, is significantly smaller than the spacing between spring pins, s. The resulting

G is given[25] by

$$G = \frac{\pi}{\ln 2} t T_2(\frac{t}{s}) = 4.5324t \qquad (5.2)$$

since $T_2(\frac{t}{s}) \to 1$ as $\frac{t}{s} \to 0$.

There is an additional caveat, however. This correction factor assumes that the metal layer is infinitely long and infinitely wide in-plane. What this translates to in practical terms is that the surface under test had to have a diameter of at least an order of magnitude larger than s or else an additional correction term C must be multiplied into G, defined as

$$C_0 \left(\frac{d}{s}\right) = \left(1 + \frac{1}{\ln 2} \ln \left(\frac{1 + 3(\frac{s}{d})^2}{1 - 3(\frac{s}{d})^2}\right)\right)^{-1}. \qquad (5.3)$$

The easiest way to get around this wasto conduct the four-point measurement in the center of the full 5 cm wafer.

5.1.2 T_c measurement procedure

To perform the dipstick measurement, first a sample no larger than 3 cm square was fixed to the sample holder on the end of the dipstick using only the pressure applied by the gold spring-probe pins. With the sample holder at 25 , the four point resistivity measurement began by sourcing 100 μA of current across the outer pins and logging the voltage of the inner pins. The sample holder was then placed into the dewar's central chamber, secured, and the outer sleeve of the dewar was filled with liquid nitrogen. The dewar can be seen in Figure 5-2.

A probe on the sample holder read the current temperature of the dipstick, and during this process, the inner-pin voltage was continuously correlated to the temperature. When the liquid nitrogen brought the holder temperature below 115 K, we began adding liquid helium to the dewar's central chamber. We flowed liquid helium into the central chamber until the probe read 4.2 K, at which point we continued flowing for another 90 sec to ensure an adequate bath. At this point, the temperature of the sample could be controlled by raising and lowering the dipstick, which moved it through varying vapor pressures above the helium bath. Using this method, the temperature was slowly modulated around 4 to
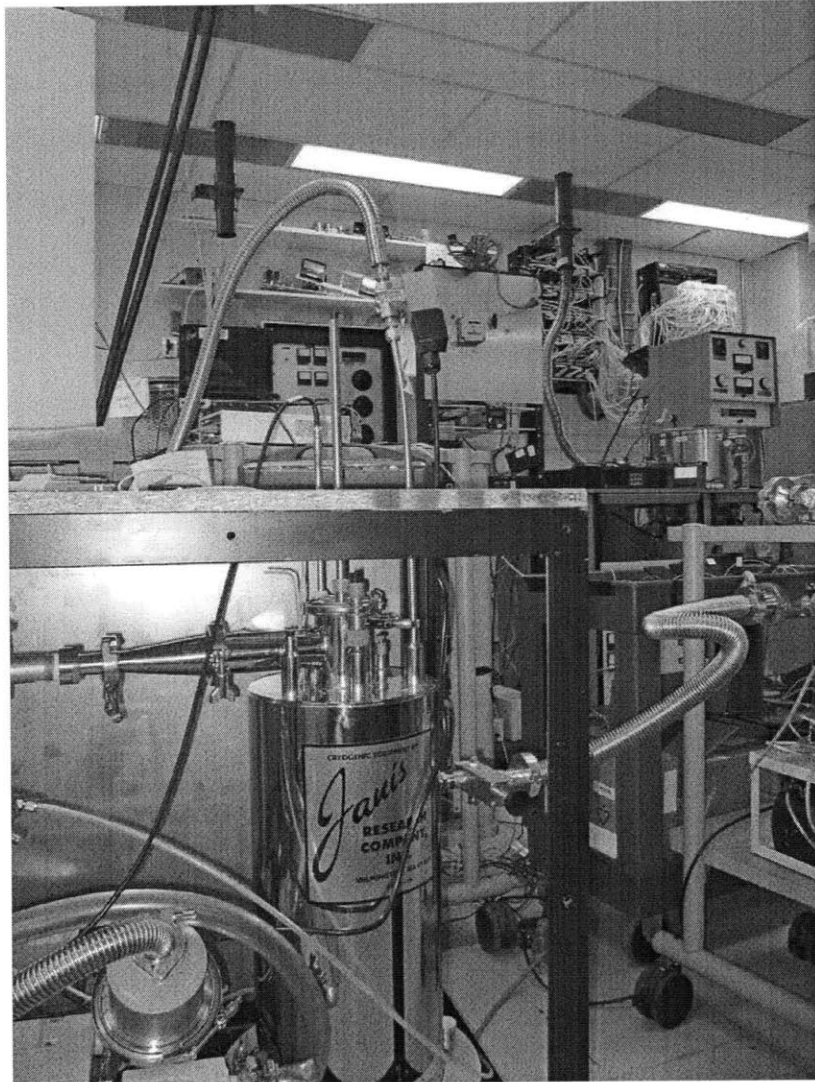
Figure 5-2: Dewar and dipstick setup for cooling down samples

30 K, to find the critical current and ensure that any lag between the temperature and resistivity readings was negligible versus the rate of heating and cooling. Once data was done being collected, the dipstick was either removed from the dewar for sample retrieval, or left to warm slowly. Either way, the sample was not used again, as it had just endured cooldown and the pressure of gold spring-probe pins andwas no longer a suitable surface for fabrication.

5.2 Device Characterization with the Probe Station

The majority of the testing done in this thesis was performed in the cryogenic probe station. Although not as well shielded as a complete immersion system, the probe station allowed for rapid testing of multiple devices on a single chip. Using only a network analyzer, we were able to gather all the relevant data necessary to determine quality factors of the devices under test. The procedure for cooling the station down was very involved and is described in section 5.2.3.

5.2.1 Probe station apparatus

The probe station we used for testing was a Desert Cryogenics TTP4, with a cold head capable of reaching 1.4 K. The probes we used were Picoprobe Model P-14-6204-O4, shown in Figure 5-4. The system is pictured in Figure 5-3, and consists of a cylindrical central chamber with the cold head area in its center. The cold head lies in the center of the chamber, and as the coldest point of the system it is where the sample holder and sample is mounted. Since the probe station is open-cycle, the cold head is cooled down with an external dewar of helium. A roughing pump is also attached to the plumbing of the system to lower the pressure beneath the cold head and allow the station to reach temperatures below 4.2 K.

The chamber was16 cm in diameter with a window in its cap and bellows protruding from its sides. It is shown open in Figure 5-5. A camera was positioned above the system, pointing down through the chamber window. Its lens system combined viewing and lighting into one optical column, which allowed us to illuminate and zoom in on the areas we were
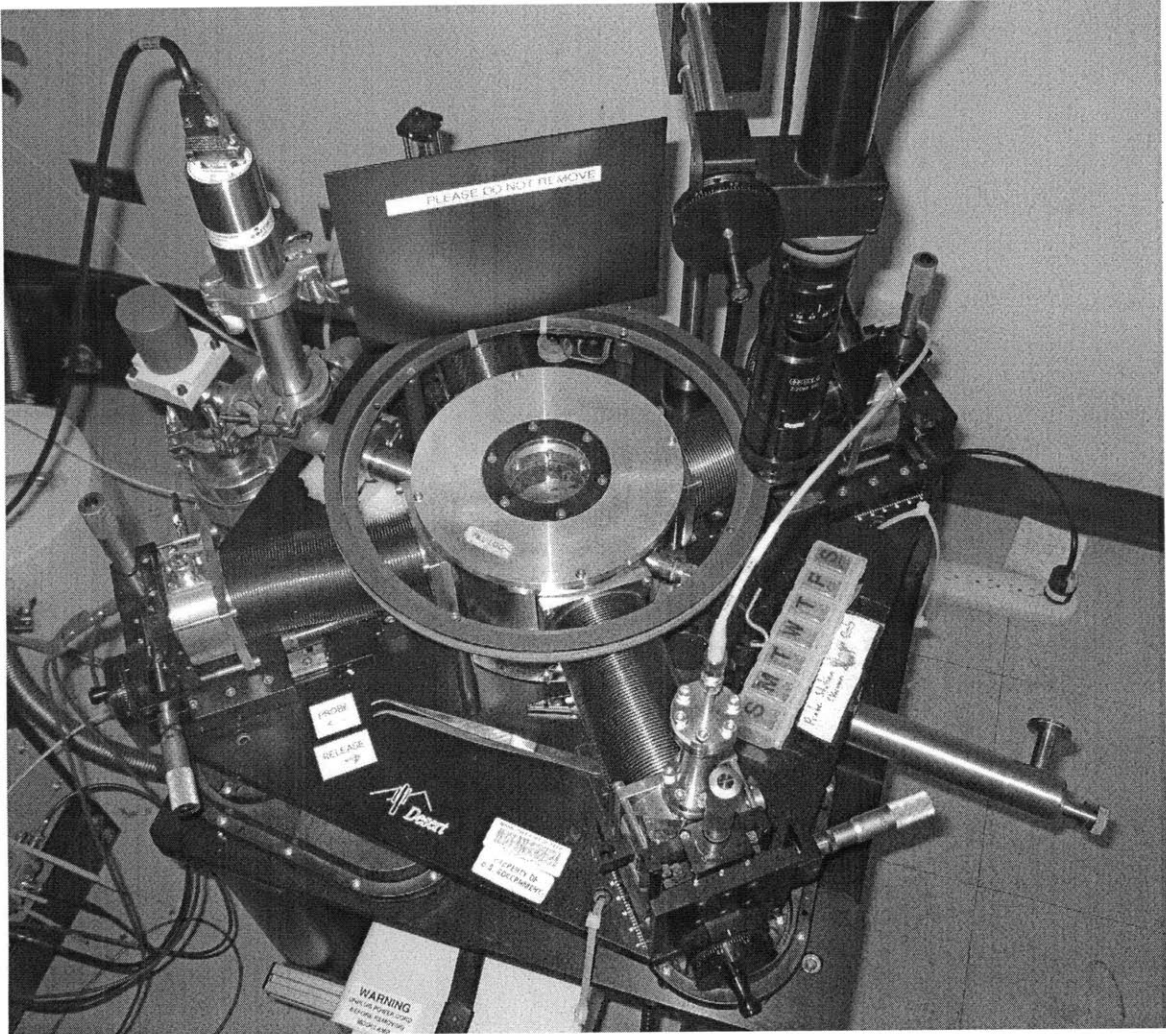
Figure 5-3: The exterior of the probe station
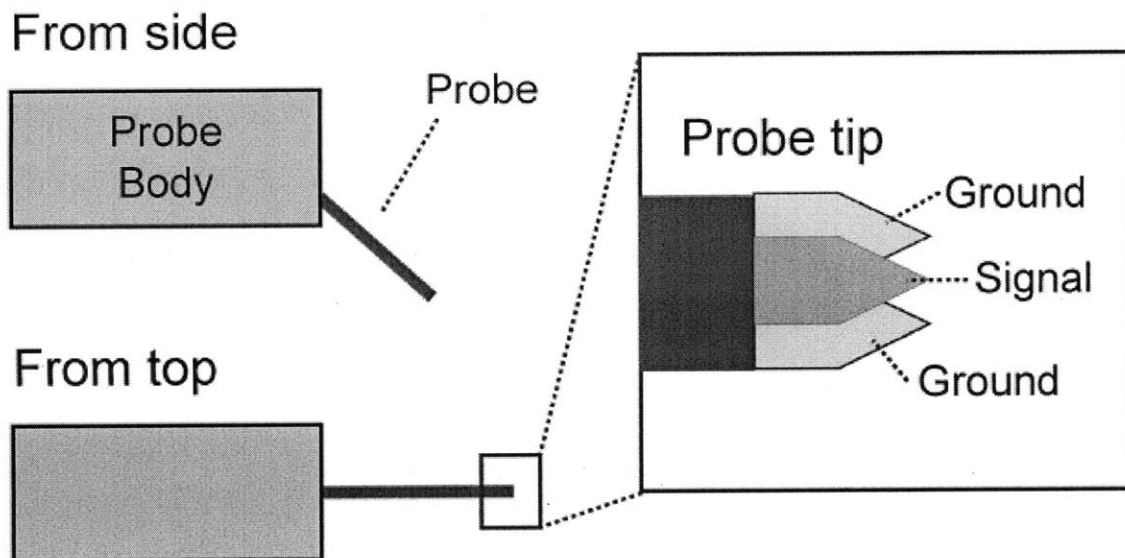
Figure 5-4: Schematic of the probes used in the TTP4 probe station. The left shows the shape of the body, the right shows a closeup of the probe tip and its ground-signal-ground setup

probing. Since the structures we probed are on the scale of microns, the camera zoom was necessary to navigate the probes around the sample.

Each of the bellows protruding from the chamber contained an arm, with the probe at its end. The probe was rigidly fixed to the end of the arm, but the arm was capable of movement in all three cartesian axes, allowing the probe tip to contact different areas of a sample fixed to the cold head. A stainless steel microwave feedthrough that ran the length of the arm delivers microwave power from the outside world to the probe. To sink the heat carried by this connection, the probe body was connected to the cold head by a thick copper braid.

Surrounding the cold head inside the chamber was the radiation shield, a stainless steel radiation barrier with an infrared-absorbing window aligned with the chamber window for visibility. It acted as a thermal boundary between the 300 K chamber walls and the sample. This radiation shield had ports in line with each bellows, through which the probes could reach the cold head.
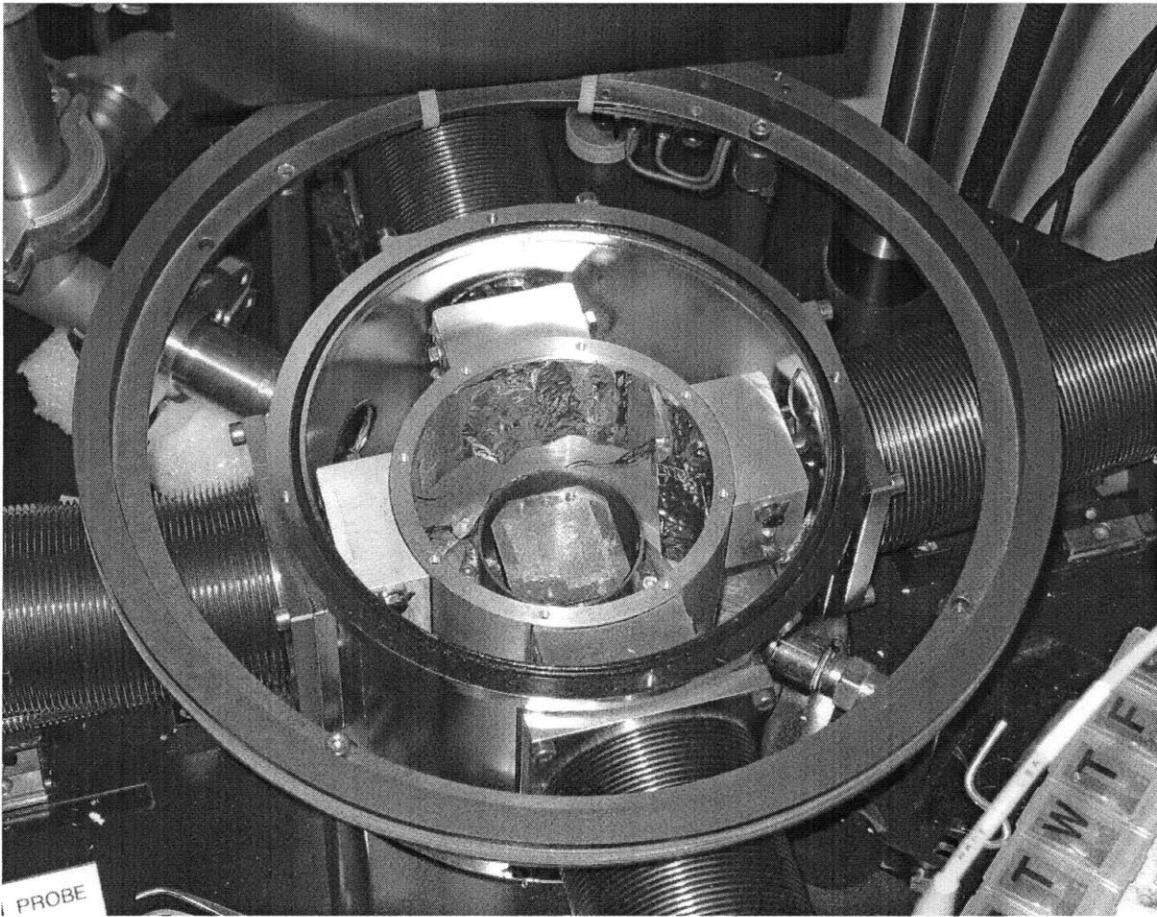
Figure 5-5: The interior of the probe station

5.2.2 Measurement electronics

Through a GPIB interface, we collected data about the system through three devices. A four-point temperature sensor mounted on the cold head was connected via four-wire cryogenic cable [1] to a Lakeshore 321 temperature controller. An additional sensor, monitoring the temperature of the radiation shield and sample holder, was connected to a Lakeshore 331 temperature controller. Lastly, to determine the microwave characteristics of the resonators, we connected an HP 8722C Network Analyzer to the SMA connectors on the station's feedthrough.

The network analyzer had two ports, and was able to capture reflection and transmission scattering parameters over a range of 50 MHz to 40 GHz. Since our first resonance occurred around 3 GHz, we typically looked at a range inclusive of the first three resonances, 1 to 10 GHz. To determine the quality factor of high-Q devices, we sampled data around resonance at the network analyzer's maximum resolution, 100 KHz. We collected the real and imaginary portions of the scattering parameters versus frequency. The data was collected using a Prologix serial GPIB-USB Controller connected to a laptop computer. We wrote two layers of MATLAB code, the first to interface with the Prologix interface, and on top of that a second layer specific to the 8722C, to facilitate the collection of the GPIB data. This code is available in Appendix A.

Since we fabricated $\lambda/2$ resonators, we were most interested in collecting the transmission scattering parameter S_{21} with the network analyzer. Tests showed that the devices reflected a large majority of the power incident upon them, even at resonance, and so the dips that should be visible in reflection (S_{11}) measurements were only a small fraction of the total power returned, making them difficult to analyze. This was likely due to mismatched input impedances, or with the overall loss of the system. Although we initially experimented with external amplifiers and filters, once we had a reliable fabrication process, the transmitted power around resonance was high enough to make external amplification and filtering unnecessary.

The primary sources of microwave loss in the system were from the stainless steel

---

[1]From Lakeshore

feedthroughs and the probes themselves. The probe insertion loss graph is shown in Figure 5-6. More critically, the feedthroughs have stainless steel shields and cores which minimized thermal loading of the probes, but which are also highly lossy at microwave frequencies. When the system is cold, one end of the feedthrough is cold, and the other is outside, making it impossible to isolate the feedthrough for microwave characterization. We were able, however, to place the probes very close together (signal tips within 10 microns) on a transmission line, essentially shorting probes together. The result is shown in Figure 5-7, and its maximums represent the total loss of the probe station. The large dips in the figure are due to the extra capacitance of the transmission line. In future tests, a specific calibration structure with only small contact pads–not the center of a 20 mm TL–should be implemented on the device surface.
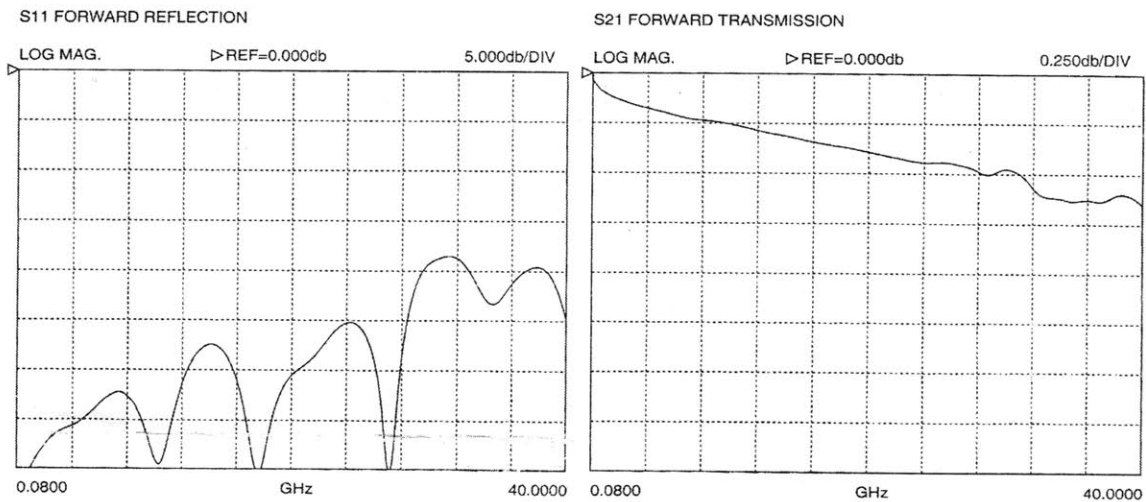
Figure 5-6: S_{21} and S_{11} characteristics of the probe.

5.2.3 Testing procedure

Mounting the sample

Finding a method to mount the sample on the cold head required a number of revisions to our sample holder. Initially we began with a vertically mounted sample, and fixed a Si mirror to the holder at 45°to be able to see the sample with the camera. This system was first adopted because the other users of the probe station were using the vertical mounting
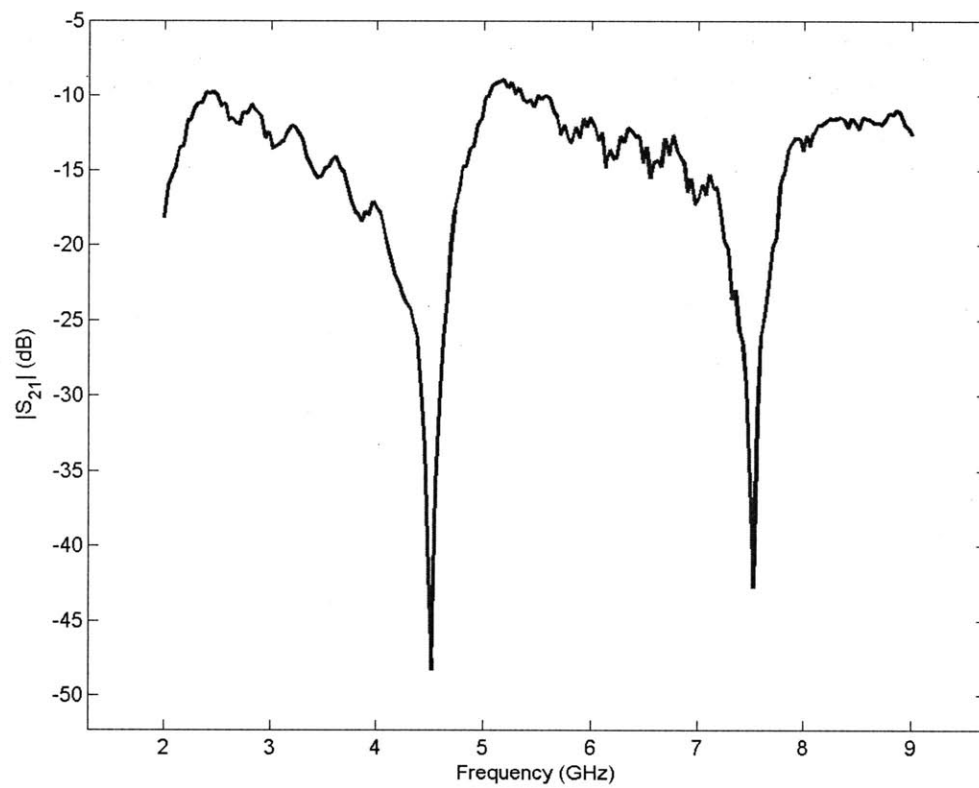
Figure 5-7: S_{21} characteristics when the probes are nearly touching.

system. It had two large drawbacks, however: the upside-down T shape of the holder was structurally poor at cooling the sample, and it was extremely difficult to align the Si mirror with the camera to see the vertically-mounted sample.

The first major revision was removing the vertical mounting area and making the sample holder a single rectangular block of OFHC copper, upon which the sample would be affixed by conductive silver paint. This improved the visibility of the sample greatly through the camera, as we no longer required an aligned mirror. Unfortunately, for several tests after this change we struggled with highly inconsistent results. Eventually, we determined that the sample was superconducting only in certain areas, and that there were localized warm spots due to poor and uneven heat conduction through the silver paint. We changed the type of silver paint to SPI Silver Paste Plus, more suitable for cryogenic heat conduction, and the testing consistency improved. Eventually, we settled on creating a frame that would press the sample down onto the holder to be able to use indium as a conduction layer, since the silver paste had a thermal conductivity of 4 W/mK versus that of indium, 81.8 W/mK. Between the sample and sample holder we put a layer of 0.25 mm indium for heat conduction. The holder assembly can be seen in Figure 5-8. To further increase the contact of the indium, after the sample was fixed in place by the frame, the entire holder setup was baked at 90° C for 5 min.

Cooling down the probe station

In order to cool down the probe station, first all of the air had to be pumped out of it to minimize gas condensation. Once the sample holder was mounted on the cold head, the turbo was engaged until the chamber reached a pressure below 3×10^{-5} mbar. Once under vacuum, we flowed liquid helium into the cryogen plumbing. Initially, the needle valve underneath the station was closed to force the helium to cool the radiation shield. If the cold head was cooled first, the remaining gas in the chamber was prone to condensing on the sample. Once the radiation shield dropped below 50 K, the needle valve was opened slightly and the helium roughing pump was turned on to cool down the cold head. The cooling reached equilibrium when the cold head reached 1.4 K and the radiation shield dropped below 30 K. Bringing the probe station from vented to cryogenic temperatures
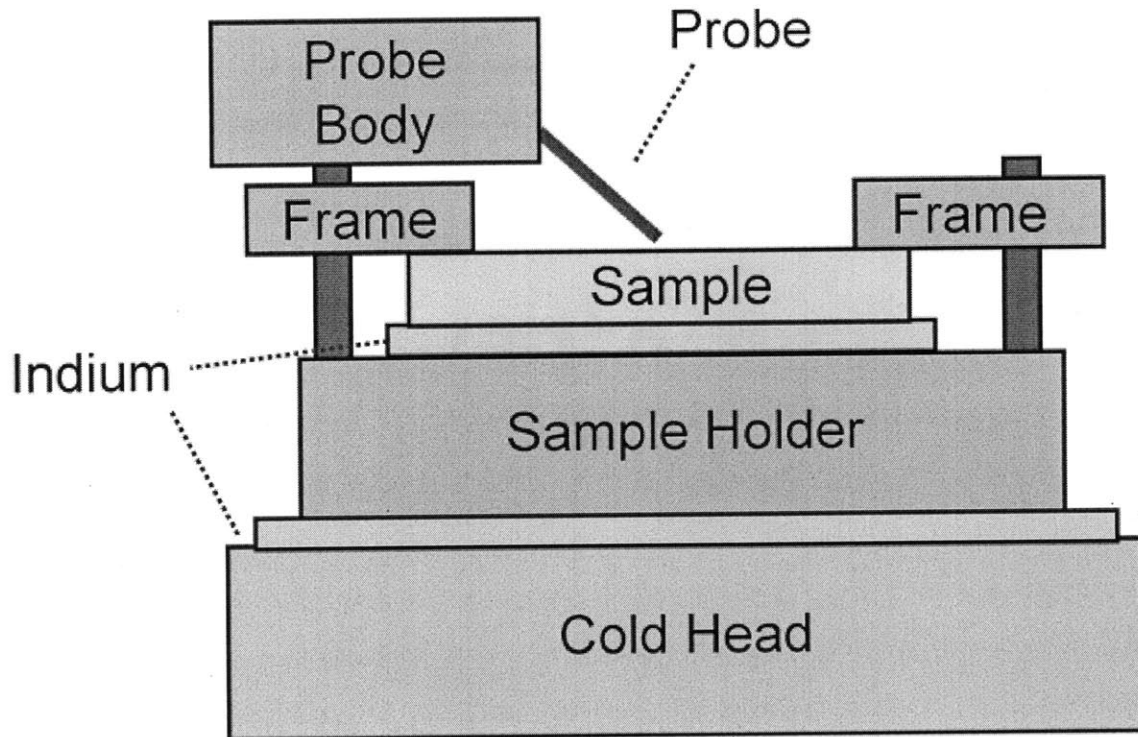
Figure 5-8: Layout of the cold head and sample holder assembly

took about 3 hours and 10-15 L of liquid helium. The cold head could remain stable at
1.4±0.1 K at a cost of about 5 L/hour.

Testing the devices

Once the system had reached the desired temperature, the probes were maneuvered to test
individual devices. Once aligned with the device, the probe signal fingers were dropped onto
either end of the center electrode of the resonator, and DC multimeter tests were performed
before taking any microwave measurements. First, we measured the resistance between the
ground and signal pin of the probes. A finite resistance indicated the presence of a short.
Next, the two signal lines of the probes were checked for connectivity to ensure the center
electrode was unbroken.

Once the DC tests were complete, the probes were moved to the device contact pads for
microwave characterization. We attached the network analyzer to the system using double-
shielded 50 Ω SMA cables. The cable impedances were calibrated out of the measurement

using the 8722C calibration kit. Unfortunately due to the fixed nature of the feedthroughs, their loss and impedances could not be calibrated against. Typically we took a large sweep with 1601 points on the network analyzer, from 1 to 10 GHz. At this resolution, resonances with a quality factor of 10 to 10,000 were plainly visible. The spectrum was recorded in real and imaginary components of S_{21} for this range, and again after zooming in on specific resonances. The results are discussed in the following chapter.

Chapter 6

Results

Once we had fabricated and tested the devices, we then needed to characterize them. This was done by fitting parameters to each set of data from the network analyzer, particularly Q and f_0. We found that we had achieved a maximum Q of 1.2×10^4 in the probe station. Additionally, by simulating the coupling capacitances we were able to fit identical devices with varying coupling capacitances against their expected lumped-element behavior, and found good agreement. We also have assembled data from a resonator with light shining on it, and examined the relationship between the light and the sample temperature. The temperature readings were unfortunately unreliable for much of the time during which this data was taken, but in the future we plan to move to a cryogenic immersion testing setup in a dewar, at which point we should have much more accurate temperature readings and control.

6.1 Fitting Quality Factors

Fitting quality factors from S_{21} was performed in MATLAB in three steps. First, we estimated Q using by setting the maximum magnitude point as f_0, and then finding the halfway point on either side of the peak to get the FWHM, Δf, and then calculating the quality factor using $Q = f_0/\Delta f$. This estimate of f_0 and Q were then passed as initial parameters to the least-squares nonlinear solver *lsqnonlin*, fitting the equation

$$S_{21} = \frac{A}{1 + iQ\left(\frac{f}{f_0} - 1\right)} + Bf + C \qquad (6.1)$$

against the data provided. In this equation, A, B, C, f_0, and Q are the parameters for the lorentzian. The lorentzian fit given in the above equation was used because of its noise tolerance and excellent results when compared with other fitting methods[19][4].

The least-squares solver typically found a good fit, but visual inspection revealed it often found a local minima that did not quite align with the data points. To get slightly better fits, the resulting parameters from *lsqnonlin* were then fed into another optimization function, *fminsearch*. The fit parameters found by *fminsearch* are the ones used in all discussion of values in this chapter.

6.2   High-Q Results

Using the testing setup detailed in Chapter 5, we successfully tested resonators with a maximum Q of 1.2×10^4. The results for the first resonance around 3 GHz are shown in Figure 6-1. Since the network analyzer had poor resolution relative to the bandwidth, there are few data points around the peak, but the sides of the peak were detailed enough to generate a good fit.

The same resonator is shown in Figure 6-2, demonstrating the circle fit technique on the real-imaginary axes. It serves to highlight how even a small number of points can be fitted to define the shape of the entire transmission spectrum.

This resonator had a center strip width of 7µm and gaps of 4µm, and the quality factors of it were significantly higher than those of the the resonators with larger center strip widths. We have not yet gathered data on center strip width versus quality factor, but the literature[27] suggests that smaller center strips yield higher quality factors.

6.3   Q vs C_κ

By calculating the distributed element values as described in section 3.2 and simulating the coupling capacitances, we were able to plot the expected relationship between coupling
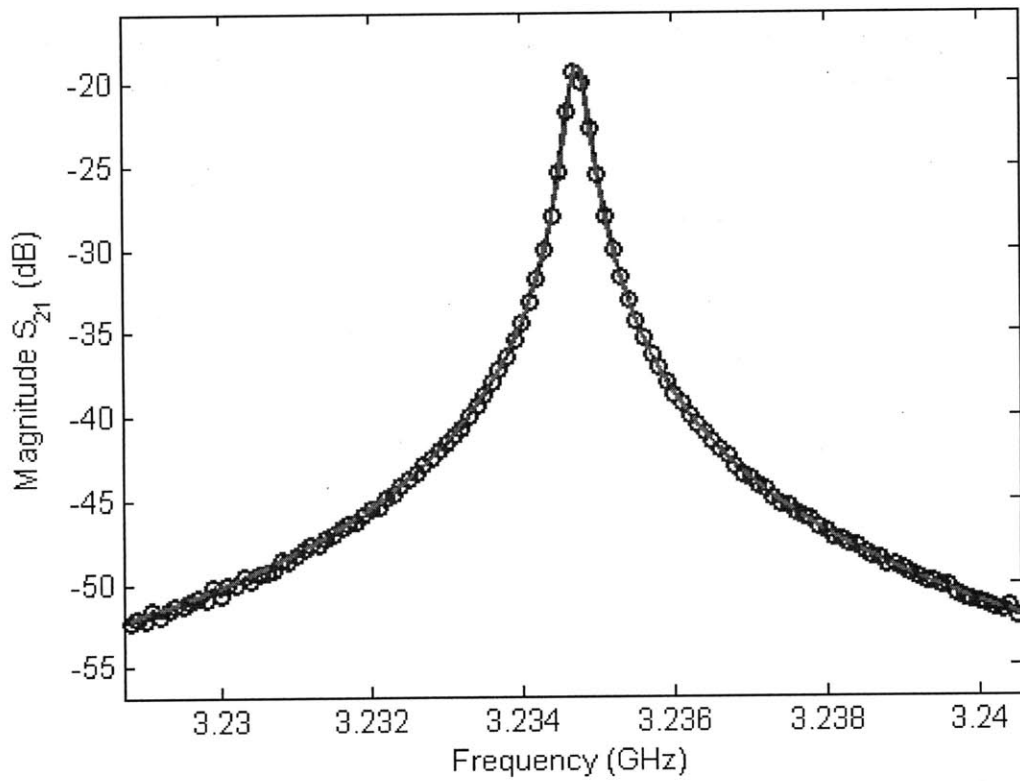
Figure 6-1: First resonance of the highest-Q resonator we tested. Experimental data points are in blue, the lorentzian fit is in red with parameters $f_0 = 3.235$ GHz, Q = 12,630.
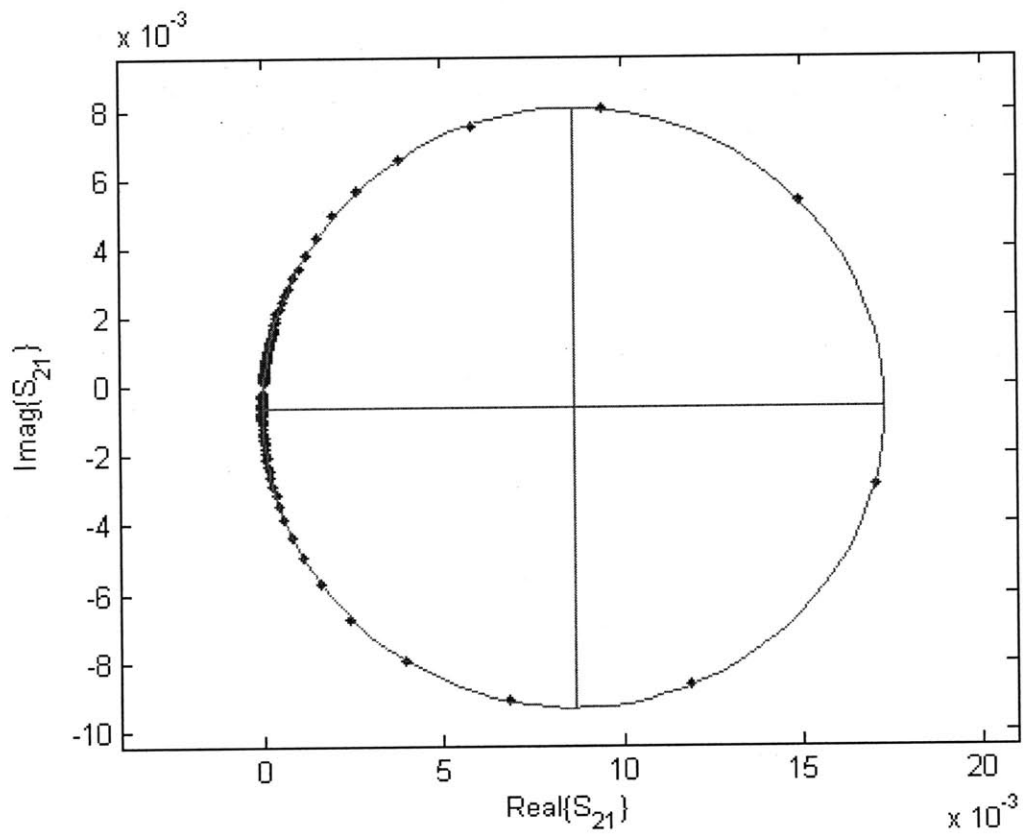
Figure 6-2: First resonance of the highest-Q resonator we tested, fitted in polar coordinates to a circle

capacitance and Q, as discussed in Chapter 3 and compare them with our experimental results. The results are shown in Figure 6-3. They show good agreement with the shape of the expected results, but some of the experimental values of Q were off by a factor of 2 or more. This could be due to a number of reasons, foremost among which is the uncertainty in temperature. At the temperatures we were working with, $T/T_c \approx 0.5$, and so small variations of sample temperature translate into large variations of Q. Other factors, such as altered input impedance R_L or different lumped-element values of L or C are unlikely, since they would not vary so much from resonator without significant fabrication issues which were not observed.

The CPW calculations gave geometric inductance and capacitance per unit length of $L_l^m = 8.16$ nH/m and $C_l^m = 3.36$ pF/m. The resonators were 20.2 mm long, yielding a total L of 1.64 nH (for the first resonance) and C of 1.39 pF. Examining the highest values of Q, we assume Q_{int} to be 5400, and from Eq. (3.21) we arrived at an R value of 186 kΩ.

6.4   Dipstick Cooldown Results

The resistivity measurements during cooldown for Nb and NbN are shown in Figure 6-4 and Figure 6-5 respectively. The graphs clearly delineate the transition between the normal conducting state and superconducting state, showing us the critical temperature T_c for each material. The residual resistance ratio was not found, however. This is because an automatic voltage readout was unavailable at the time of experiment and the temperature was not logged during the early stages of cooldown. Additionally, the graphs are in terms of the centerpin voltage rather than the calculated resistivity ρ; at the time of the experiment it was not clear that the geometry and dimensions of the sample needed to taken into account, so arbitrary shaped samples were used that are too small to be negligible compared to the pin spacing s.

6.5   Superconducting Transmission Line Measurements

As a basis for testing in the probe station, next to every set of resonators we fabricated we also put a transmission line with the same geometry (without the coupling capacitors)
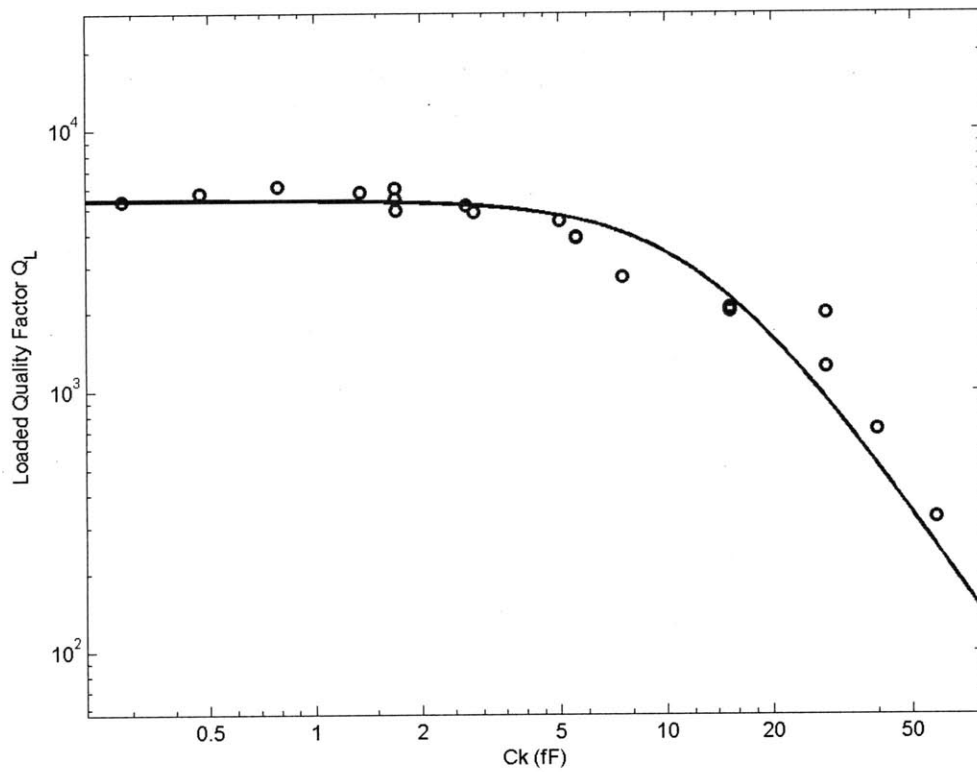
Figure 6-3: Coupling capacitance vs. resonator quality factor. The circles are measured Q values with simulated C_κ values. The solid line represents the expected fit calculated from lumped-element values.
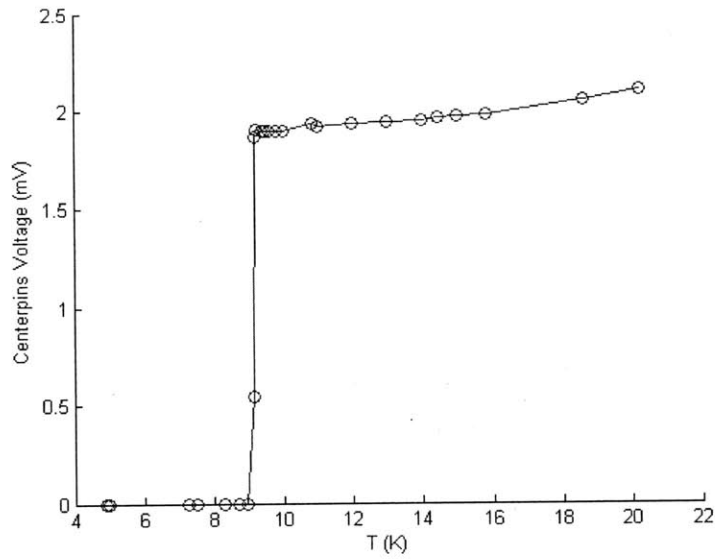
Figure 6-4: Four-point resistance measurement of 200nm Nb @ 100mA, Tc = 9.15K
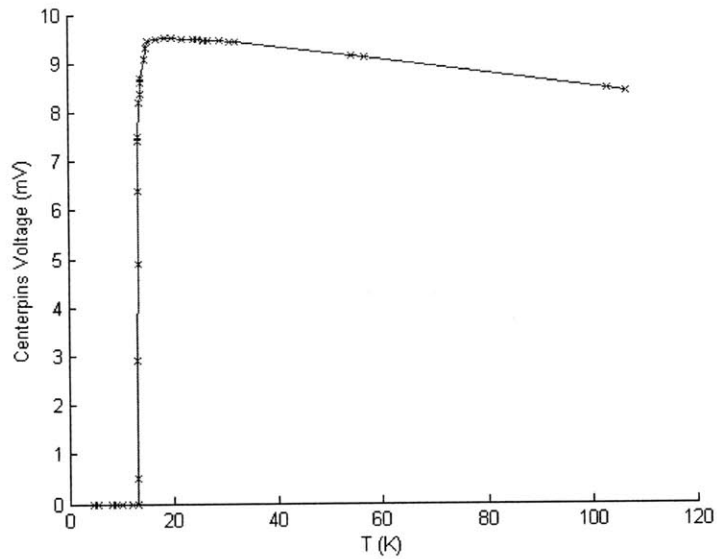
Figure 6-5: Four-point resistance measurement of 200nm NbN @ 1mA, Tc = 13.25K

for reference purposes. Just like the resonators, they were designed with a characteristic impedance of $Z_0 = 50\ \Omega$. The results are shown in Figure 6-6, and they indicate the system is behaving as expected. The slope of the magnitude is constant with some fluctuation due to the uncalibrated impedance mismatch of the system causing voltage standing waves.
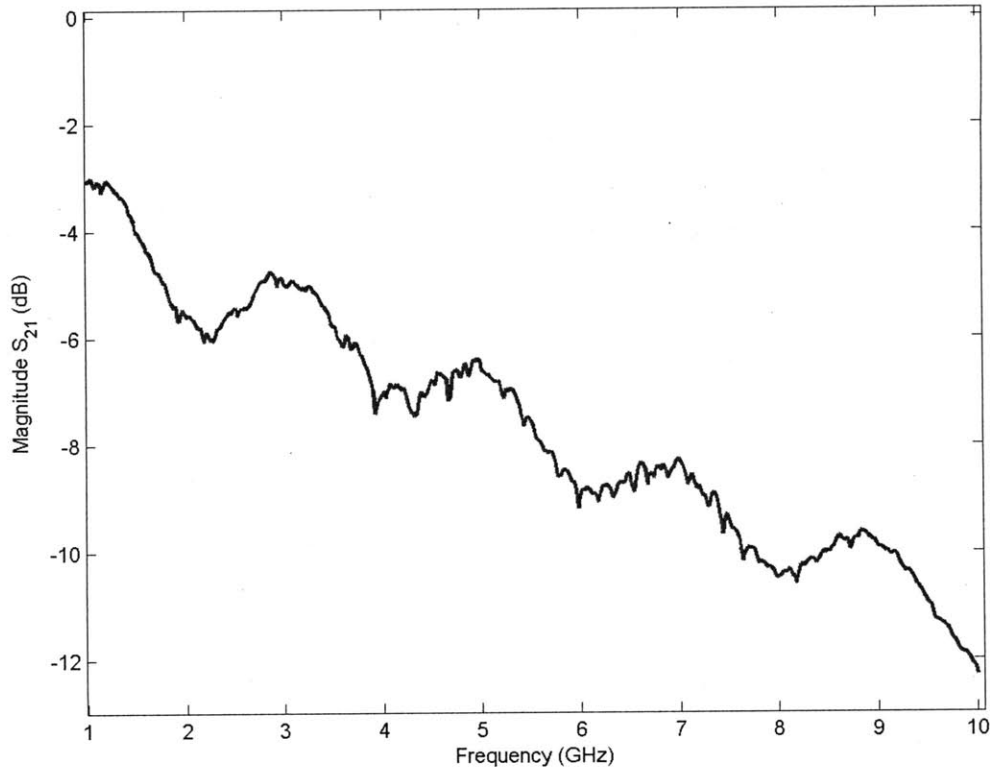
Figure 6-6: S_{21} of a superconducting transmission line. It has a length of 20 mm. Its centerstrip has a gap of 10 µm, and width of 18 µm

6.6   Results with Varying Incident Light intensities

To investigate the effects of light incident on the devices, we took the variable light source from the camera and directed it through the chamber window. We then measured the light reflected back out of the window with a photodiode, taking that to be approximately proportional to the intensity incident on the devices. The results are shown in Figure 6-7. We also graphed the change in Q and f_0 with the light intensity, shown in Figure 6-8 and Figure 6-9.
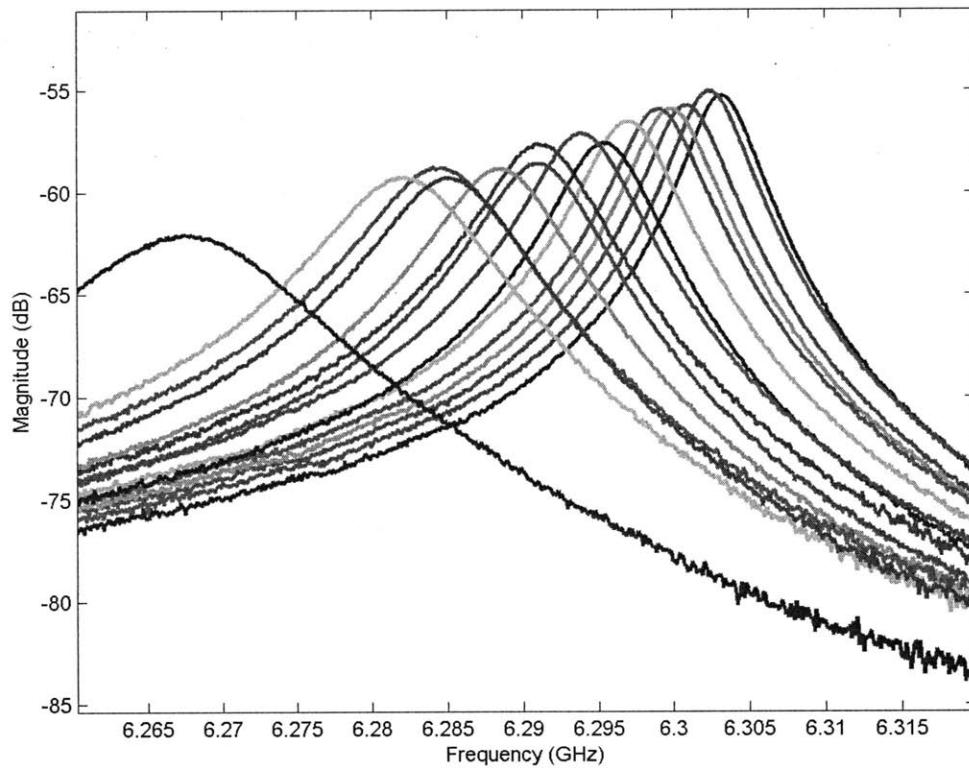
Figure 6-7: Second resonances with varying intensities of light incident on the device
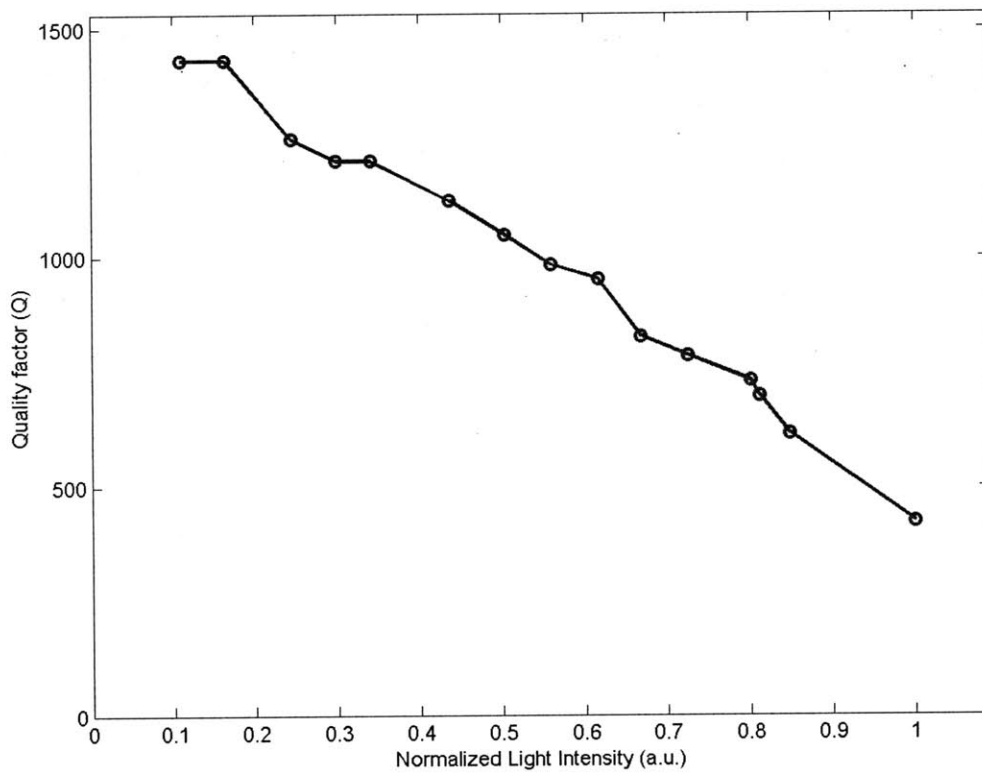
Figure 6-8: Quality factor versus intensity of light incident on the device
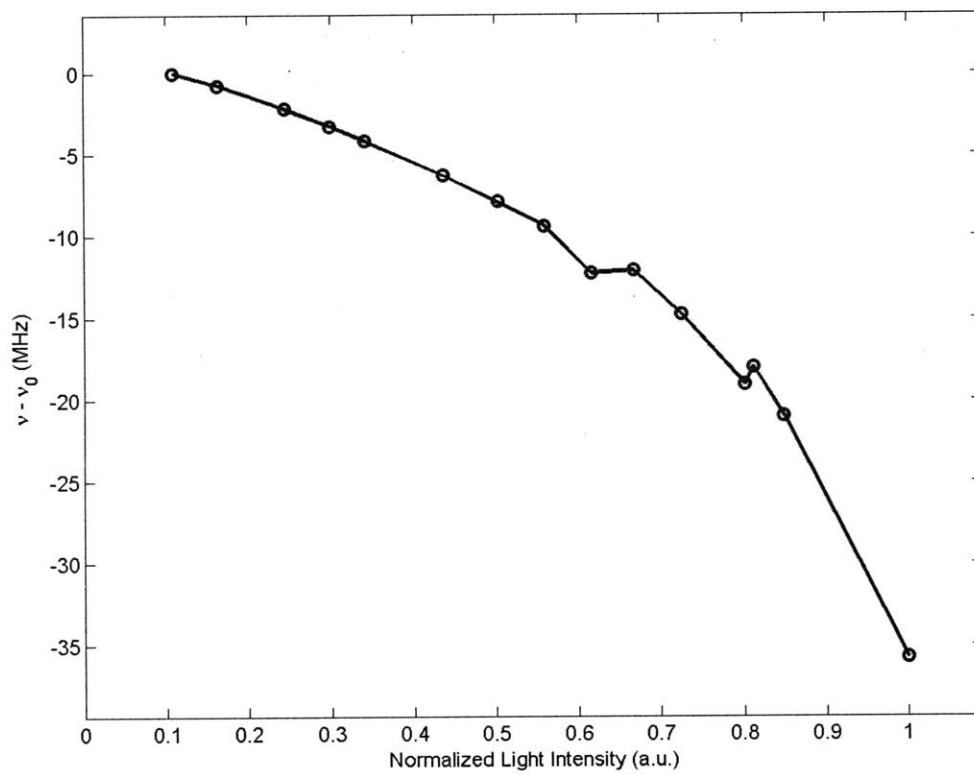
Figure 6-9: Resonant frequency versus intensity of light incident on the device

The datapoints in both graphs have the same relationship versus light intensity as they do versus temperature, which led us to believe that the two were proportional. Although we did not have accurate temperature readings for this data, we show this proportionality in Figure 6-10, where we have fitted this light-temperature relationship for f_0 by hand. Using computed values of L_m, L_s, and g, we determined α and then selected the temperature range over which the data fit Eq. (3.30) best, in this case 3 to 5 K.
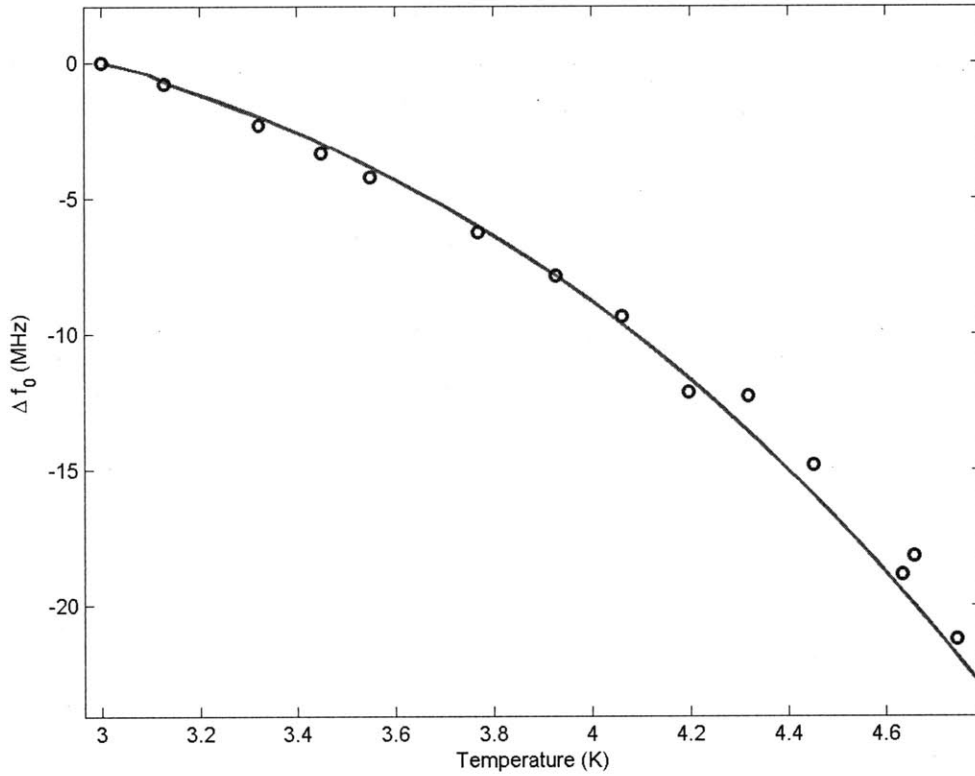
Figure 6-10: Change in resonant frequency f_0 versus temperature change caused by light incident on a niobium resonator. In red is the calculated Δf_0, while the blue circles are data points

Appendix A

MATLAB 8722C GPIB Interface Code

```
%%%%%%%%%%%%%%%%%%%%%%%%%%%%%%%%%%%%%%%%%%%%%%%%%%%%%%
% File:   get_8722c_sweep.m
% Creation Date:   28-Sep-2009
% Modification Date: 01-Nov-2009
% Author: Adam McCaughan (amcc@mit.edu)
%
% Grabs whatever data is on the screen currently by switching it to single
% mode, collecting the data, then returning it to continuous

function [F,M] = get_8722c_sweep(s1)


% Since the 8722C is on GPIB address 7
serial_write(s1, '++addr 7')


fstart = strread(serial_write(s1, 'STAR?;'));
fspan = strread(serial_write(s1, 'SPAN?;'));
fstop = strread(serial_write(s1, 'STOP?;'));
```

```matlab
numpts = strread(serial_write(s1, 'POIN?;'));

f_inc = fspan/(numpts-1);

F = fstart+((1:numpts)-1).*f_inc;

F = F';


serial_write(s1, 'OPC?;SING;');

serial_wait(s1,300);

serial_write(s1, 'FORM4;');

serial_write(s1, 'OUTPFORM;');

pause(2);  % pause while it readies output

M = serial_readn(s1, numpts);

M = slist2nums(M, '%n,%n');

M = M(:,1);



%%%%%%%%%%%%%%%%%%%%%%%%%%%%%%%%%%%%%%%%%%%%%%%%%%%%%%%%%%%%

% File:   run_8722c_sweep.m

% Date:   28-Sep-2009

% Author: amcc@mit.edu

%

% Takes in a frequency start (GHz) and stop, number of points to sample

% between those two, and returns the frequency & magnitude data from them

% Needs s1 the serial object

%

% Returns magnitude data in the format [Mag1 Mag2 ... MagN] where N = navgs


function [F,M] = run_8722c_sweep(s1, navgs, fstart, fstop, numpts)


% Since the 8722C is on GPIB address 7

serial_write(s1, '++addr 7')
```

```
if (nargin > 2)

    % Ensure proper formatting for GPIB command

    fstart = roundn(fstart,-4)*10000;

    fstop = roundn(fstop,-4)*10000;


    numptsstr = ['POIN ' num2str(numpts) ';'];

    startstr = ['STAR ' num2str(fstart) '.E+5;'];

    stopstr = ['STOP ' num2str(fstop) '.E+5;'];


    serial_write(s1, numptsstr);

    serial_write(s1, startstr);

    serial_write(s1, stopstr);

end


if (nargin < 2)

    navgs = 1; end


for c = 1:navgs

    [F,M(:,c)] = get_8722c_sweep(s1);

    disp(['Trace ' num2str(c) ' out of ' num2str(navgs)]);

end


response = serial_write(s1, 'CONT;');

response = serial_write(s1, '++loc');
```

%%%

```
%%%%%%%%%%%%%%%%%%%%%%%%%%%%%%%%%%%%%%%%%%%%%%%%%%%%%

% File:    serial_interactive.m

% Date:    28-Sep-2009

% Author: amcc@mit.edu

%

% Makes a giant (~800k) buffer for reading serial data and runs

% a continuous loop interacting with the serial port


maxPts = 1601;

bytesperline = 512;

warning off serial:fscanf:unsuccessfulRead

if ~isempty(instrfind)

    fclose(instrfind); end

s1 = serial('COM3','BaudRate',115200, ...

    'InputBufferSize',maxPts*bytesperline,'TimeOut',0.2);

fopen(s1)


while 1

    s1input = input('Input text: ','s');

    response = serial_write(s1, s1input);

    disp(['response: ' response])

end




%%%%%%%%%%%%%%%%%%%%%%%%%%%%%%%%%%%%%%%%%%%%%%%%%%%%

%%%%%%%%%%%%%%%%%%%%%%%%%%%%%%%%%%%%%%%%%%%%%%%%%%%%%

% File:    serial_readn.m

% Date:    28-Sep-2009
```

```
% Author: amcc@mit.edu
%
% Takes in a serial object and returns n lines from the buffer
% as strings in a list.  If n is not defined, it returns one line
% not in a list.  Terminates if the line received is empty


function response = serial_readn(s1, n)


% Wait for the transmission to finish
BA = s1.BytesAvailable;
pause(0.5)
while (s1.BytesAvailable > BA)
    BA = s1.BytesAvailable;
    disp(['[serial_readn] Collecting data... Bytes in buffer:  ' num2str(BA)]);
    pause(1)
end


if (nargin < 2)
    response = fscanf(s1,'%s');
else
    for c = 1:n
        response{c} = fscanf(s1,'%s');
        if isempty(response{c}), break, end
    end
end


%%%%%%%%%%%%%%%%%%%%%%%%%%%%%%%%%%%%%%%%%%%%%%%%%%%%%%%

%%%%%%%%%%%%%%%%%%%%%%%%%%%%%%%%%%%%%%%%%%%%%%%%%%%%%%%%%
```

```matlab
% File:    serial_wait.m
% Date:    28-Sep-2009
% Author: amcc@mit.edu
%
% Takes in a serial object and waits up to n seconds for a single message
% (ie a signal message that some process is done)



function response = serial_wait(s1, n)


if (nargin < 2)
    n = 1000; end

for c = 1:n
    pause(.2)
    response = fscanf(s1,'%s');
    if ~isempty(response), break, end
    disp(['[serial_wait] No response, waiting 1s... ' num2str(c) ' elapsed'])
    pause(.8)
end


%%%%%%%%%%%%%%%%%%%%%%%%%%%%%%%%%%%%%%%%%%%%%%%%%

%%%%%%%%%%%%%%%%%%%%%%%%%%%%%%%%%%%%%%%%%%%%%%%%%%%
% File:    serial_write.m
% Date:    28-Sep-2009
% Author: amcc@mit.edu
%
% Writes a string to a serial object.  If an output argument is
% defined, returns the first line of response
```

```matlab
function response = serial_write(s1, s1input)

    fprintf(s1,s1input)

    if nargout > 0

        pause(0.1)

        response = serial_readn(s1); end

end
```

%%

%%

% File: slist2nums.m

% Date: 29-Sep-2009

% Author: amcc@mit.edu

%

% Takes in a list of strings, reads them according to form and outputs

% the result

```matlab
function nums = slist2nums(slist, form)


for c = 1:length(slist)

    s = slist{c};

    nums(c,:) = textscan(s, form, 'CollectOutput',1);

end

nums = cell2mat(nums);
```

%%%

Appendix B

MATLAB Surface Impedance Numerical Solver Code

```
%%%%%%%%%%%%%%%%%%%%%%%%%%%%%%%%%%%%%%%%%%%%%%%%%%%%%%
function [Zs qq K Y] = surimp6(M,T,F,numqpts)


% MAYBE Write out exponential form for Regime III to speed things up
% TODO: Change Zsint to eqn B.8 p148 Gao to remove singularity



u0 = 4*pi*1e-7;
w = 2*pi*F;



% Regime I:    q << (max([1/M.xi0 1/M.l_mfp]))
% Should be constant for q << 5e7


% Regime III:  q >> (max([1/M.xi0 1/M.l_mfp]))
% Should be constant for q >> 5e7
```

```matlab
figure(82); close(82); figure(82);

qregime2 = max([1/M.xi0 1/M.l_mfp]);

K0 = mbkernel6(qregime2/2e4, w, T, M);

Y0 = log(1+K0./(qregime2/(2e4)).^2);

semilogx(qregime2/2e4,Y0,'bo');


global qstore Kstore Ystore

qstore = []; Kstore = []; Ystore = [];


maxint = 100; rtol = 1e-6;

QY = quadgk(@(q)mbkloop(q,w,T,M), 0, Inf,'MaxIntervalCount',maxint,'RelTol',rtol,'AbsTol'


Zs = 1i*u0*w*pi/QY;

qq = qstore;

K = Kstore;

Y = Ystore;


function Y = mbkloop(qq,w,T,M)

global qstore Kstore Ystore


qregime2 = max([1/M.xi0 1/M.l_mfp]);

K0 = mbkernel6(qregime2/2e4, w, T, M);


figure(82)

K = zeros(size(qq));

Y = zeros(size(qq));

for c = 1:length(qq)

    if qq(c) < qregime2/2e4

        K(c) = K0;
```

83

```matlab
        Y(c) = log(1+K0./qq(c).^2);
    else
        K(c) = mbkernel6(qq(c), w, T, M);
        Y(c) = log(1+K(c)./qq(c).^2);
    end
%       disp(['q = ' num2str(qq(c)) ', K = ' num2str(K(c))])
        hold on; semilogx(qq(c),Y(c),'r.'); hold off
end
qstore = [qstore qq];
Kstore = [Kstore K];
Ystore = [Ystore Y];
[qstore qi] = sort(qstore);
Kstore = Kstore(qi);
Ystore = Ystore(qi);


%%%%%%%%%%%%%%%%%%%%%%%%%%%%%%%%%%%%%%%%%%%%%%%%%%%%%%%%%%%%

%%%%%%%%%%%%%%%%%%%%%%%%%%%%%%%%%%%%%%%%%%%%%%%%%%%%%%%%%%%%


function out = mbkernel6(q, w, T, M)
heV = 4.135e-15;    % Planck constant [eV*s]
hbareV = heV/(2*pi);    % Rationalized planck constant [eV*s]
[hw D D1 D2 b a1 a2 ap am gE fE fEhw] = mbkparams(1,1,w,T,M);

if size(q,2) > size(q,1)
    q = transpose(q); end

rtol = 1e-5;
maxint = 100600;
```

```
% infin = D*5;

% d = D*rtol;


% E = linspace(max([(D-hw+d) -D]), D-d, numpts);

% Q1 = trapz(E,Krealint1(E,q,w,T,M));

% [EM qM] = meshgrid(E,q);

% Q1 = trapz(E,Krealint1(EM,qM,w,T,M),2);

[Q1 err1] = quadgk(@(E)Krealint1(E,q,w,T,M), max([(D-hw) -D]), D,'MaxIntervalCount',maxin


if (hw < 2*D)

    Q2 = zeros(size(Q1));

else

%     E = linspace(D-hw, -D, numpts);

%     [EM qM] = meshgrid(E,q);

%     Q2 = trapz(EM,Krealint2(EM,qM,w,T,M),2);

%     Q2 = trapz(E,Krealint2(E,q,w,T,M));

    [Q2 err2] = quadgk(@(E)Krealint2(E,q,w,T,M), D-hw, -D,'MaxIntervalCount',maxint,'RelT


end


[Q3 err3] = quadgk(@(E)Krealint3(E,q,w,T,M), D, Inf,'MaxIntervalCount',maxint,'RelTol',rt

[Q4 err4] = quadgk(@(E)Krealint4(E,q,w,T,M), D, Inf,'MaxIntervalCount',maxint,'RelTol',rt


% E = logspace(log10(D+d), log10(D+d) + log10(1.0001), numpts);

% E = [E logspace(log10(D+d) + log10(1.0001), log10(infin), numpts)];

% [EM qM] = meshgrid(E,q);

% Q3 = trapz(E,Krealint3(EM,qM,w,T,M),2);

% Q4 = trapz(E,Krealint4(EM,qM,w,T,M),2);

% Q3 = trapz(E,Krealint3(E,q,w,T,M));

% Q4 = trapz(E,Krealint4(E,q,w,T,M));
```

```
if (hw < 2*D)

    Q5 = zeros(size(Q1));

else

%     E = linspace(D-hw, -D, numpts);

%     [EM qM] = meshgrid(E,q);

%     Q5 = trapz(E,Kimagint5(EM,qM,w,T,M),2);

%     Q5 = trapz(E,Kimagint5(E,q,w,T,M));

    [Q5 err5] = quadgk(@(E)Kimagint5(E,q,w,T,M), max([(D-hw) -D]), -D,'MaxIntervalCount',

end

% E = linspace(D+d, infin, numpts);

% [EM qM] = meshgrid(E,q);

% Q6 = trapz(E,Kimagint6(EM,qM,w,T,M),2);

% Q6 = trapz(E,Kimagint6(E,q,w,T,M));

[Q6 err6] = quadgk(@(E)Kimagint6(E,q,w,T,M), D, Inf,'MaxIntervalCount',maxint,'RelTol',rt


%

%

% disp(['Integral 1) ' num2str(Q1) ', err of ' num2str(err1/Q1*100) '%']);

% disp(['Integral 2) ' num2str(Q2) ', err of ' num2str(err1/Q2*100) '%']);

% disp(['Integral 3) ' num2str(Q3) ', err of ' num2str(err1/Q3*100) '%']);

% disp(['Integral 4) ' num2str(Q4) ', err of ' num2str(err1/Q4*100) '%']);

% disp(['Integral 5) ' num2str(Q5) ', err of ' num2str(err1/Q5*100) '%']);

% disp(['Integral 6) ' num2str(Q6) ', err of ' num2str(err1/Q6*100) '%']);


Kreal = 3./(q*hbareV*M.nu0*M.L0^2).*(Q1+1./2.*Q2-Q3+Q4);

Kimag = 3./(q*hbareV*M.nu0*M.L0^2).*(-1./2.*Q5+Q6);


out = transpose(Kreal + 1i.*Kimag);
```

```
function plotdebug(E,Y,n)

figure(n); plot(E,abs(Y),'b-',E,real(Y),'r-',E,imag(Y),'g-');

% disp(['Sum ' num2str(n) ') real: ' num2str(sum(real(Y))) ', imag: ' num2str(sum(imag(Y)

% global EE YY

% EE = E;

% YY = Y;

% pause


function Y = Krealint1(E,q,w,T,M)

[hw D D1 D2 b a1 a2 ap am gE fE fEhw] = mbkparams(E,q,w,T,M);



Y = (1-2.*fEhw) ...

    .* ((E.^2+D^2+hw*E)./(sqrt(D^2-E.^2).*sqrt((E+hw).^2-D^2)) .* R(a2,a1+b) + S(a2,a1+b)

% Y = real(Y); % Since it's an integral for the real part

% plotdebug(E,Y,1);


function Y = Krealint2(E,q,w,T,M)

[hw D D1 D2 b a1 a2 ap am gE fE fEhw] = mbkparams(E,q,w,T,M);



Y = (1-2.*fEhw).*((gE+1).*S(am,b) - (gE-1).*S(ap,b));

% plotdebug(E,Y,2);


function Y = Krealint3(E,q,w,T,M)

[hw D D1 D2 b a1 a2 ap am gE fE fEhw] = mbkparams(E,q,w,T,M);



Y = (1-fE-fEhw).*(gE-1).*S(ap,b);

% plotdebug(E,Y,3);
```

```
function Y = Krealint4(E,q,w,T,M)
[hw D D1 D2 b a1 a2 ap am gE fE fEhw] = mbkparams(E,q,w,T,M);


Y = (fE - fEhw).*(gE+1).*S(am,b);
% plotdebug(E,Y,4);




function Y = Kimagint5(E,q,w,T,M)
[hw D D1 D2 b a1 a2 ap am gE fE fEhw] = mbkparams(E,q,w,T,M);


Y = (1-2.*fEhw).*((gE+1).*R(am,b)+(gE-1).*R(ap,b));
% plotdebug(E,Y,5);




function Y = Kimagint6(E,q,w,T,M)
[hw D D1 D2 b a1 a2 ap am gE fE fEhw] = mbkparams(E,q,w,T,M);


Y = (fE-fEhw).*((gE+1).*R(am,b)+(gE-1).*R(ap,b));
% plotdebug(E,Y,6);




function out = R(a,b)
% Updated 5/19/2010


s = b-1i*a;
out = real(-s/2+(s.^2+1)/2.*atan(1./s));
% nx = zeros(size(a));
% nx(b.^2+a.^2-1 < 0) = ones(size(nx(b.^2+a.^2-1 < 0)));
%
```

```
% out = -b./2 + a.*b./4.*log((b.^2+(1+a).^2)./(b.^2+(1-a).^2)) ...
%       + 1./4.*(1+b.^2-a.^2).*(atan(2.*b./(b.^2+a.^2-1)) + nx.*pi);



% Eqn A.25 from Appendix A, Gao thesis p145
function out = S(a,b)
% Updated 5/19/2010


s = b-1i*a;
out = imag(-s/2+(s.^2+1)/2.*atan(1./s));


% nx = zeros(size(a));
% nx(b.^2+a.^2-1 < 0) = ones(size(nx(b.^2+a.^2-1 < 0)));
%
% out = a./2 - a.*b./2.*(atan(2.*b./(b.^2+a.^2-1))+nx.*pi) ...
%       + 1./8.*(1+b.^2-a.^2).*log((b.^2+(1+a).^2)./(b.^2+(1-a).^2));


function fE = fermi(E,T)
kbeV = 8.617e-5;      % eV./K


if (T==0)
    fE = zeros(size(E));
    fE(E<=0) = ones(size(E(E<=0)));
else
    fE = 1./(1+exp(E/(kbeV*T)));
end



function gE = g(E,hw,D,D1,D2)
```

89

```matlab
gE = (E.^2+D.^2+hw.*E)./(D1.*D2);



function [hw D D1 D2 b a1 a2 ap am gE fE fEhw] = mbkparams(E,q,w,T,M)

heV = 4.135e-15;     % Planck constant [eV*s]

hbareV = heV/(2*pi);     % Rationalized planck constant [eV*s]


hw = hbareV * w;

b = 1./(q*M.l_mfp);

D = reducedenergygap(T,M.Tc,M.D0);

D1 = sqrt(E.^2-D.^2);

D2 = sqrt((E+hw).^2-D.^2);

a1 = D1./(hbareV*M.nu0*q);

a2 = D2./(hbareV*M.nu0*q);

ap = a1+a2;

am = a2-a1;

gE = g(E,hw,D,D1,D2);

fE = fermi(E,T);

fEhw = fermi(E+hw,T);




%%%%%%%%%%%%%%%%%%%%%%%%%%%%%%%%%%%%%%%%%%%%%%%%%%%

%%%%%%%%%%%%%%%%%%%%%%%%%%%%%%%%%%%%%%%%%%%%%%%%%%%
% As described on p24 Gao thesis, section 2.2.6
% Table data taken from Muhlschlegel for T/Tc > 0.18
% Adapted verbatim from SuperMix code in supercond.cc



function D = reducedenergygap(T,Tc,D0)
```

```
x = T/Tc;

xmatch = 0.32;

ymatch = exp(-sqrt(3.562*xmatch)*exp(-1.764/xmatch));


% // Table of reduced energy gap vs. T/Tc, from Muhlschlegel (1959).

% // Table starts at x = T/Tc = 0.18, and goes in steps of dx = 0.02

ratiotable =    [1.0,     0.9999, 0.9997, 0.9994, 0.9989, ...

    0.9982, 0.9971, 0.9957, 0.9938, 0.9915, ...

    0.9885, 0.985,  0.9809, 0.976,  0.9704, ...

    0.9641, 0.9569, 0.9488, 0.9399, 0.9299, ...

    0.919,  0.907,  0.8939, 0.8796, 0.864,  ...

    0.8471, 0.8288, 0.8089, 0.7874, 0.764,  ...

    0.7386, 0.711,  0.681,  0.648,  0.6117, ...

    0.5715, 0.5263, 0.4749, 0.4148, 0.3416, ...

    0.2436, 0.0];


% static double gap_supcond(double x)

% {

%    // the argument x = T/Tc; check if x is physical

%    if(x < 0. || x >= 1.) return(0.0);   // return gap of zero

if (x>1) || (x<0), error('Nonphysical x'); end


%

%    // if T/Tc < 0.04, reduced energy gap is 1.0, to better than 1 part in 10^22

%    if(x < 0.04) return(1.0);   // return gap of 1.0

if (x<0.04), ratio = 1;


%    // if T/Tc <= xmatch, we use an analytic expression to extend the gap table;

%    //   ( which uses k Tc ~= Delta(0)/1.764; c.f. Tinkham )
```

```
%
%    static const double xmatch = 0.32;   // xmatch must be a multiple of 0.02, >= 0.18
%    static const double ymatch = exp(-sqrt(3.562*xmatch)*exp(-1.764/xmatch));
%    if(x <= xmatch) return(exp(-sqrt(3.562*x)*exp(-1.764/x)));   //
%    3.562==2*Pi/1.764
elseif (x < xmatch)
    ratio = exp(-sqrt(2*pi/1.764*x)*exp(-1.764/x));


%    // if we get here, we interpolate between data points to calculate gap, taking
%    // sqrt(1 - T/Tc) dependence near the gap into account.
%
%    int index = static_cast<int>(floor((x-0.18)/0.02));   // index into ratio[]
%    double xl = index*0.02 + 0.18,
%            xu = xl + 0.02,
%            yl = ((xl > xmatch) ? ratio[index] : ymatch)/sqrt(1.-xl),
%            yu = (index < 40) ? ratio[index+1]/sqrt(1.-xu) : 1.74;
%                    // Behavior near Tc - see Tinkham, eqn. 2-54.
else
    index = floor((x-0.18)/0.02);
    xl = (index-1)*0.02 + 0.18; % index-1 since in C++ first point is 0
    xu = xl + 0.02;

    if (xl > xmatch)
        yl = ratiotable(index)/sqrt(1-xl);
    else
        yl = ymatch/sqrt(1-xl);
    end

    if (index < 40)
        yu = ratiotable(index+1)/sqrt(1-xu);
```

```matlab
    else
        yu = 1.74;
    end


    ratio = sqrt(1 - x) * (yl + (yu-yl)*(x-xl)/(xu-xl));
end


D = D0*ratio;
```

%%

%%%

%%

%%

%%

Bibliography

[1] A. André, D. DeMille, J. M. Doyle, M. D. Lukin, S. E. Maxwell, P. Rabl, R. J. Schoelkopf, and P. Zoller. A coherent all-electrical interface between polar molecules and mesoscopic superconducting resonators. *Nature Physics*, 2(9):636–642, 2006.

[2] P B Antohi, D Schuster, G M Akselrod, J Labaziewicz, Y Ge, Z Lin, W S Bakr, and I L Chuang. Cryogenic ion trapping systems with surface-electrode traps. *The Review of scientific instruments*, 80(1):013103, January 2009.

[3] Waseem Bakr. *Towards a cryogenic planar ion trap for Sr-88*. PhD thesis, MIT, 2006.

[4] P.R. Bevington. *Data Reduction and Error Analysis for the Physical Sciences*. McGraw-Hill, New York, 1969.

[5] S. Calatroni. 20 Years of experience with the Nb/Cu technology for superconducting cavities and perspectives for future developments. *Physica C: Superconductivity*, 441(1-2):95101, July 2006.

[6] RG Chambers. The anomalous skin effect. *Proceedings of the Royal Society of London. Series A,*, 215(1123):481–497, December 1952.

[7] R.E. Collin. *Foundations of Microwave Engineering*. IEEE Press, New York, 2 edition, 2000.

[8] J Gao. *The physics of superconducting microwave resonators*. Phd, California Institute of Technology, 2008.

[9] M. Goppl, A. Fragner, M. Baur, R. Bianchetti, S. Filipp, J. M. Fink, P. J. Leek, G. Puebla, L. Steffen, and A. Wallraff. Coplanar waveguide resonators for circuit quantum electrodynamics. *Journal of Applied Physics*, 104(11):113904, July 2008.

[10] I. Hahn, P. Day, B. Bumble, and H. G. LeDuc. Recent Results of a New Microwave SQUID Multiplexer. *Journal of Low Temperature Physics*, 151(3-4):934–939, January 2008.

[11] G Hammer, S Wuensch, K Ilin, and M Siegel. Ultra high quality factor resonators for kinetic inductance detectors. *Journal of Physics: Conference Series*, 97(Eucas 2007):012044, 2008.

[12] Jaroslaw Labaziewicz, Yufei Ge, Paul Antohi, David Leibrandt, Kenneth Brown, and Isaac Chuang. Suppression of Heating Rates in Cryogenic Surface-Electrode Ion Traps. *Physical Review Letters*, 100(1):13001, January 2008.

[13] Francesco Marsili. Marsili Thesis Chapter III : Fabrication. pages 41–76, 2009.

[14] B.W. Maxfield and WL McLean. Superconducting penetration depth of niobium. *PHYS REV*, 139(5):15151522, 1965.

[15] Benjamin A. Mazin. *Microwave kinetic inductance detectors*. Phd, California Institute of Technology, 2005.

[16] C S Menon and V S Pankajakshan. Electrical conductivity and transition temperature of NbN thin films. *Bulletin of Materials Science*, 9(3):187–191, August 1987.

[17] W. Paul. Electromagnetic traps for charged and neutral particles. *Reviews of Modern Physics*, 62(3):531540, 1990.

[18] C. Pearson, D. Leibrandt, W. Bakr, W. Mallard, K. Brown, and I. Chuang. Experimental investigation of planar ion traps. *Physical Review A*, 73(3):1–12, March 2006.

[19] P.J. Petersan and S.M. Anlage. Measurement of resonant frequency and quality factor of microwave resonators: Comparison of methods. *Journal of Applied Physics*, 84(6):3392, 1998.

[20] R. Pöpel. Surface impedance and reflectivity of superconductors. *Journal of Applied Physics*, 66:5950, 1989.

[21] D.M. Pozar. *Microwave engineering*. Wiley-IEEE Press, 3 edition, February 2009.

[22] DI Schuster. Circuit quantum electrodynamics. 2007.

[23] S. Seidelin, J. Chiaverini, R. Reichle, J. Bollinger, D. Leibfried, J. Britton, J. Wesenberg, R. Blakestad, R. Epstein, D. Hume, W. Itano, J. Jost, C. Langer, R. Ozeri, N. Shiga, and D. Wineland. Microfabricated Surface-Electrode Ion Trap for Scalable Quantum Information Processing. *Physical Review Letters*, 96(25):1–4, June 2006.

[24] Rainee N. Simons. *Coplanar Waveguide Circuits Components & Systems*. Wiley-IEEE Press, 1 edition, March 2001.

[25] H. Topsoe. *Geometric Factors in Four Point Resistivity Measurement*. 2nd edition, 1968.

[26] L. J. van Der Pauw. A method of measuring specific resistivity and Hall effect of discs of arbitrary shape. *Philips Res. Rep.*, 13(1-9), 1958.

[27] H Wang, M Hofheinz, J Wenner, M Ansmann, R C Bialczak, M Lenander, Erik Lucero, M Neeley, A. D. O'Connell, D Sank, M Weides, A N Cleland, and John M Martinis. Improving the Coherence Time of Superconducting Coplanar Resonators. 93106:3, 2009.

[28] Shi-ping Zhou, A Jabbar, Jia-shan Bao, Ke-qin Wu, and Bian-jun Jin. Analytical solution of MattisBardeen theory for surface impedance of superconductors. *Journal of Applied Physics*, 71(6):2789, 1992.

[29] J Zmuidzinas. Superconducting Microresonator Detectors. pages 1–12, 2008.